Effects of radiation reaction in the interaction between cluster media and high intensity lasers in the radiation dominant regime

Natsumi Iwata,[1,a)] Hideo Nagatomo,[1] Yuji Fukuda,[2] Ryutaro Matsui,[3] and Yasuaki Kishimoto[3]

[1]*Institute of Laser Engineering, Osaka University, 2-6 Yamadaoka, Suita, Osaka 565-0871, Japan*
[2]*Kansai Photon Science Institute (KPSI), National Institute for Quantum and Radiological Science and Technology (QST), 8-1-7 Umemidai, Kizugawa, Kyoto 619-0215, Japan*
[3]*Graduate School of Energy Science, Kyoto University, Gokasho, Uji, Kyoto 611-0011, Japan*

Interaction between media composed of clusters and high intensity lasers in the radiation dominant regime, i.e., intensity of 10^{22-23} W/cm^2, is studied based on the particle-in-cell simulation that includes the radiation reaction. By introducing target materials that have the same total mass but different internal structures, i.e., uniform plasma and cluster media with different cluster radii, we investigate the effect of the internal structure on the interaction dynamics, high energy radiation emission, and its reaction. Intense radiation emission is found in the cluster media where electrons exhibit non-ballistic motions suffering from strong accelerations by both the penetrated laser field and charge separation field of clusters. As a result, the clustered structure increases the energy conversion into high energy radiations significantly at the expense of the conversion into particles, while the total absorption rate into radiation and particles remains unchanged from the absorption rate into particles in the case without radiation reaction. The maximum ion energy achieved in the interaction with cluster media is found to be decreased through the radiation reaction to electrons into the same level with that achieved in the interaction with the uniform plasma. The clustered structure thus enhances high energy radiation emission rather than the ion acceleration in the considered intensity regime. *Published by AIP Publishing.* [http://dx.doi.org/10.1063/1.4954152]

I. INTRODUCTION

With the advent of innovative laser technologies, the intensity of ultrashort high power lasers reaches to the order of 10^{21} W/cm^2.[1,2] In laser–matter interaction in such a regime, electrons are accelerated to relativistic energies within a few laser cycle period. Such a high intensity laser–matter interaction has opened up various applications, e.g., high energy particle acceleration,[3,4] generation of intense radiations from tera-heltz[5,6] to X- and gamma-rays,[7–10] fast ignition-based laser fusion,[11] and neutron production.[12]

Today, higher intensities of 10^{22-25} W/cm^2 are expected to be achieved by developing laser peak power to multi-petawatt and focusing it to the level of the diffraction limit.[13,14] In this regime, the energy of radiation from electrons accelerated by the intense laser field reaches to the range of gamma-ray.[15,16] Accordingly, damping of electron energy by the radiation friction force, i.e., the radiation damping, is not negligible in the interaction dynamics. It is reported that even for laser–matter interactions with the laser intensity in the order of 10^{22} W/cm^2, the energy loss by radiation reaction becomes effective to the laser energy absorption.[17] Laser–plasma interaction in such a radiation dominant regime has a potential to be a source of high-power gamma-ray in the level of terawatt to petawatt with tailored plasma targets.[9,10]

Here, the state and structure of target materials are a key ingredient in determining the interaction, and have to be

chosen properly according to the purpose. Among the various materials, cluster and cluster medium, i.e., a medium composed of multi-clusters, are interested owing to their high energy absorption and unique optical properties.[18,19] High harmonic generation and its resonant enhancement are the typical examples, which are resulted from dipole moment excitation by the laser field in expanding clusters.[20–23] Propagation of laser field by the cluster mode (slow mode), which is attributed to the polarization of clusters inside of the cluster medium, is also found.[24] Energetic ion generations using clusters are studied intensively for various applications, such as nuclear fusion by the Coulomb explosion of nano-size clusters[12,31] and generation of collimated high energy ion beam for hadron therapy.[25,26] Efficient ion acceleration up to 10–20 MeV per nucleon has been demonstrated by using a target composed of gas and clusters.[27] However, these studies for laser–cluster interaction have been so far conducted for the linear and electron relativistic regime, i.e., below 10^{21} W/cm^2.

As the laser intensity increases, it is expected that more electrons can be expelled from the cluster core in a short time scale, owing to the large Lorentz force and also the relativistic penetration of the laser field. The latter leads to the ideal Coulomb explosion of larger clusters, e.g., micro-meter size for laser intensity in the order of 10^{22} W/cm^2, and then generates more energetic ions.[28] In our previous study, we have investigated the fundamental dynamics and ion acceleration processes in the interaction between cluster media and high intensity laser fields in the regime of 10^{22-24} W/cm^2.[29] In this regime, ions gain relativistic energies by the radiation

a)iwata-n@ile.osaka-u.ac.jp

pressure acceleration[30] associated with the Coulomb explosion. We have found that higher maximum energy of ions can be obtained in the cluster media than that achieved by the simple piston mechanism for a solid thin foil, which is considered to be resulted from an additional acceleration by the Coulomb explosion. Here, the results in Ref. 29 were obtained without considering the radiation reaction.

However, as cluster media have been found to exhibit such a strong interaction with laser fields, the effect of radiation reaction is expected to be more important compared with the case of solid foils. In this paper, we study the effect of radiation reaction in the interaction between cluster medium and laser field in the intensity regime of 10^{22-23} W/cm^2. The corresponding normalized amplitude, which is defined as $a_0 = eE_0/m_e c\omega_L$, is $a_0 = 100-200$ where the laser wavelength is assumed to be $\lambda_L = 0.82\,\mu$m. Here, e is the elementary charge, m_e the electron mass, E_0 the amplitude of the laser electric field, c the speed of light, and $\omega_L = 2\pi c/\lambda_L$ the laser frequency. For the above purpose, we here perform numerical simulations based on the fully relativistic particle-in-cell (PIC) code EPIC3D[31] that includes the radiation reaction force in the equation of motion for electrons in terms of the Landau–Lifshitz formula.[32,33]

In Sec. II, we consider suitable cluster sizes to be considered in the simulation in order to achieve strong interactions and then radiations in the assumed intensity regime. In Sec. III, we discuss fundamental properties of the radiation emission from accelerated charges and give estimations on the power density of radiation obtained in the laser–matter interactions considered in this study. In Sec. IV, we describe the inclusion of the radiation damping effect to the PIC simulation.

To investigate the effects of clusters inside of the medium on the interaction dynamics and on the radiation damping, we here consider three kinds of targets with different configurational structures but having the same total mass in two-dimensional (2D) geometry. The systems assumed here and other simulation conditions are described in Sec. V. In Secs. VI and VII, we discuss the energy evolution and fundamental dynamics for interactions with laser fields with the peak normalized amplitude of $a_0 = 100$ and 200, respectively. In Sec. VIII, summary of the rates of energy conversion in each medium is given. In Sec. IX, we compare electron trajectories between cases with and without radiation reaction. In Sec. X, the effects of radiation damping to electron and ion energy distributions are studied. Finally, conclusions are given in Sec. XI.

II. INTERACTION OF CLUSTERS WITH LASER FIELDS

In laser–cluster interactions, larger energy absorption from laser to particles and then radiation emissions are expected compared with interactions with materials that have uniform structure as a simple foil. This advantage of clusters is attributed to the larger area of surface on which electrons can interact with the laser field that is penetrated into the medium through the inter-cluster region. On the other hand, during the interaction with laser fields, electrons are expelled from the clusters and both electrons and ions expand to be a spatially uniform distribution which will

exhibit a similar interaction property to plasmas that are distributed uniformly from the initial time. However, an ideal condition to increase the interaction, e.g., a near-critical density plasma that interact with the penetrated laser field inside of the medium, can be created during the interaction. Therefore, a key ingredient that determines the interaction property in the cluster medium is expansion of electrons during the interaction.

We consider a cluster with the initial radius of r_{cl} irradiated by a laser light of relativistic intensities $a_0 > 1$ in vacuum. The cluster consists of a fully ionized neutral plasma with ions of charge Ze and density n_i where Z is the ion atomic number. We here assume an overdense cluster $Zn_i > \gamma n_c$ so that the average density of cluster media $n_{av}(<Zn_i)$ can be near-critical, i.e., $n_{av} \sim \gamma n_c$, where γ is the relativistic factor of electron and $n_c \equiv m_e\omega_L^2/(4\pi e^2)$ is the cutoff density. As for an overdense cluster, electrons at the cluster surface are expelled at twice the laser frequency $2\omega_L$. The expelled electrons are then blown off toward the laser propagation direction by the Lorentz force, which is different from the linear regime $a_0 < 1$ where the expelled electrons come back to the original cluster area in the oscillations induced by the laser electric field.[34]

We assume that electrons have partly left the cluster and the remaining electrons distribute uniformly in a sphere of radius r_0 while ions stay immobile in the radius $r_{cl}(>r_0)$. Here, the spheres of electron and ion are assumed to be positioned concentrically. We estimate the typical kinetic energy gain of electrons from the laser field as $\epsilon_k = a_0^2 m_e c^2/4$ which corresponds to the exact solution for a relativistic electron motion in vacuum averaged by the laser frequency. As the electrons move toward the cluster edge $r = r_{cl}$, the Coulomb force $-e\mathbf{E}_{cl}$ by the remained cluster ions begins to contribute to decelerate the ejection of electrons. Hence, whether electrons can leave the cluster is determined by the ratio between the kinetic energy ϵ_k and the potential energy of the cluster $|e\phi_{cl}|$.

The electrostatic potential ϕ_{cl} at a distance r from the cluster center created by the above-assumed charge distribution in 3D geometry is given by

$$\phi_{cl}^{3D} = \begin{cases} -\dfrac{\Lambda_{3D}}{2}\left(\tilde{r}^2 + 2\tilde{r}_0^3/\tilde{r}\right) + C_1 & (r_0 \le r \le r_{cl}), \\ \Lambda_{3D}\left(1 - \tilde{r}_0^3\right)/\tilde{r} + C_2 & (r > r_{cl}), \end{cases} \tag{1}$$

and $\phi_{cl}^{3D} = 0$ for $0 < r < r_0$ where $\tilde{r} = r/r_{cl}$, $\tilde{r}_0 = r_0/r_{cl}$, $\Lambda_{3D} = 4\pi\rho r_{cl}^2/3$, $\rho = n_i Ze$, $C_1 = 2\pi\rho r_0^2$, and $C_2 = C_1 - 2\pi\rho r_{cl}^2$. The boundary condition is given by $\phi_{cl}^{3D}(r_0) = 0$. In 2D geometry where we perform PIC simulations in this study, we model the cluster by a column of radius r_{cl} in the x-y plane having infinite length in the transverse z direction. In this case, the electrostatic potential is obtained as

$$\phi_{cl}^{2D} = \begin{cases} \Lambda_{2D}(\tilde{r}_0^2 \ln \tilde{r} - \tilde{r}^2/2) + C_3 & (r_0 \le r \le r_{cl}), \\ \Lambda_{2D}(\tilde{r}_0^2 - 1)\ln \tilde{r} + C_4 & (r > r_{cl}), \end{cases} \tag{2}$$

and $\phi_{cl}^{2D} = 0$ for $0 < r < r_0$ where $\Lambda_{2D} = 2\pi\rho r_{cl}^2$, $C_3 = \pi\rho r_0^2(1 - 2\ln \tilde{r}_0)$, and $C_4 = C_3 - \pi\rho r_{cl}^2$ with the boundary condition $\phi_{cl}^{2D}(r_0) = 0$. In Fig. 1, the potentials
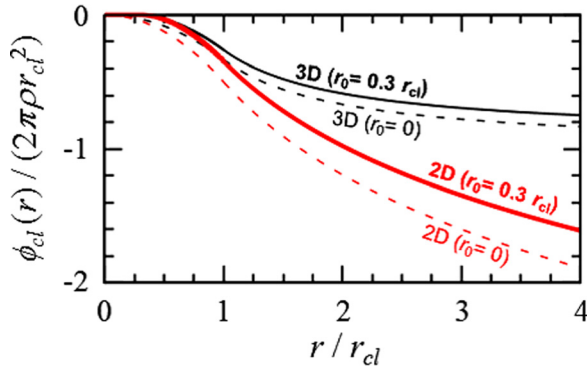
FIG. 1. Electrostatic potential ϕ_{cl} of the cluster that consists of electron and ion cores with radius r_0 and $r_{cl}(\geq r_0)$ in 2D (red) and 3D (black) geometries. By solid and dotted lines, we indicate clusters whose electrons are expelled up to radius $r_0 = 0.3r_{cl}$ and $r_0 = 0$, respectively, while the ion core with radius r_{cl} is immobile.

given in Eqs. (1) and (2) assuming two different radii of electron distribution, i.e., $r_0 = 0.3r_{cl}$ and $r_0 = 0$, are shown. It should be noted that the 2D simulation overestimates the potential energy with a logarithmic divergence of ϕ_{cl}^{2D} seen in Fig. 1 compared with the 3D case, which is also mentioned in Ref. 31.

To determine the simulation configurations, we compare the potential energy $|e\phi_{cl}^{2D}|$ and the kinetic energy of electrons ϵ_k at a position $r = r_f$, which we here assume to be the distance from cluster center to the surface of neighboring clusters in cluster media, i.e., $r_f = 3r_{cl}$, in the condition we will present in Sec. V. The ratio is given by

$$\frac{|e\phi_{cl}^{2D}(r_f)|}{\epsilon_k} = \frac{C_5 n_e}{a_0^2}\left[r_0^2\left(\ln\frac{r_f}{r_{cl}} + \frac{1}{2} + \ln\frac{r_{cl}}{r_0}\right) - C_6\right], \quad (3)$$

where $C_5 = 8\pi e^2/(m_e c^2)$ and $C_6 = r_{cl}^2(\ln(r_f/r_{cl}) + 1/2)$. In Fig. 2, we show the ratio Eq. (3) as a function of the radius
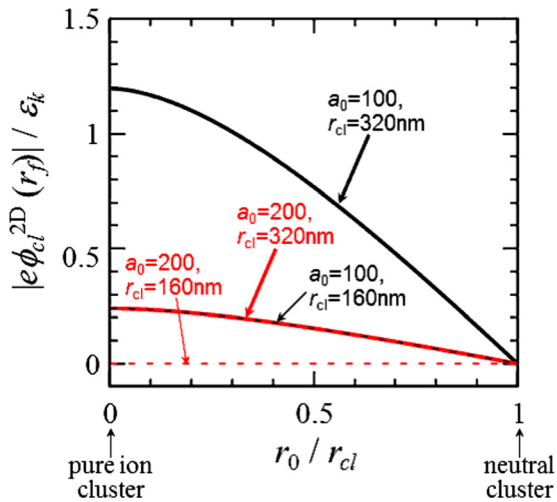

FIG. 2. Ratio of the absolute value of Coulomb potential energy $|e\phi_{cl}^{2D}|$ at $r_f = 3r_{cl}$ to electron kinetic energy ϵ_k in 2D geometry for various cluster radius r_{cl} and laser field amplitude a_0. The horizontal axis corresponds to the ratio of distribution radius of electrons, r_0, and that of ions, r_{cl}. When the value in the vertical axis is smaller than unity, i.e., $|e\phi_{cl}^{2D}| < \epsilon_k$, electrons at the surface $r = r_0$ can reach $r = r_f$ beyond the cluster edge r_{cl}.

of electron core r_0 for several a_0 and r_{cl}. The ratio denotes that the electrons can leave the cluster as long as $|e\phi_{cl}^{2D}|/\epsilon_k < 1$ is satisfied at the corresponding radius r_0. In the figure, $Z = 6$, $n_i = 1.76 \times 10^{23}\,\text{cm}^{-3}$, and $\lambda_L = 820$ nm are assumed, which are the same as those in Sec. V. For $a_0 = 100$, the potential energy $|e\phi_{cl}^{2D}|$ with radius $r_{cl} = 320$ nm (black solid line) exceeds ϵ_k when the radius of the electron core r_0 reduces to $0.3r_{cl}$. In other words, the electron core will remain with radius $r_0 \sim 0.3r_{cl}$ without being expelled by the laser field. On the other hand, for $a_0 = 200$, the cluster of $r_{cl} = 320$ nm (red solid line) keeps $|e\phi_{cl}^{2D}|/\epsilon_k < 1$ until r_0 reaches zero, and thus all the electrons will be expelled in this case. As for $r_{cl} = 160$ nm, $|e\phi_{cl}^{2D}|/\epsilon_k < 1$ is kept for all r_0 in both $a_0 = 100$ and $a_0 = 200$, which indicates that no electron core is sustained in the interaction with laser fields of $a_0 \geq 100$.

For the purpose of maximizing the interaction of electrons in cluster media with laser fields and also with cluster Coulomb fields, the suitable cluster size is considered to be that satisfies $|e\phi_{cl}^{2D}|/\epsilon_k \sim 1$ with $r_0 \sim 0$ and the average density of the cluster medium is given to be near-critical. In such a condition, a large number of electrons can interact with laser fields that has penetrated through the inter-cluster region, while the Coulomb field from cluster cores play a role in trapping the electrons in the strong interaction region.

In the above derivations, ions are assumed to be immobile. However, the quick expelling and heating of electrons could result in ion expansion by Coulomb explosion and/or charge separation during the interaction time, which will reduce the restoring force $-e\mathbf{E}_{cl}$.

III. RADIATION EMISSION FROM CHARGED PARTICLES IN THE RADIATION DOMINANT REGIME

It is known that charged particles emit radiation whenever they are accelerated. The energy of radiation by the accelerated charge can be estimated by[32] $\hbar\omega_{\text{max}} \sim \gamma^3\hbar\omega_L$. In laser–plasma interactions, the typical relativistic factor of electrons can be represented by $\gamma = (1 + a_0^2/2)^{1/2}$, which is equivalent to the averaged relativistic factor for quiver motion of electrons in linearly polarized laser electric fields. The corresponding photon energies $\hbar\omega_{\text{max}}$ are obtained as $\hbar\omega_{\text{max}} \sim 1.5$ MeV and 12.1 MeV for $\gamma \sim a_0 = 100$ and 200, respectively, which correspond to the energy range of gamma-ray. Here, the ratio between the energy of radiation and that of oscillatory motion of electrons in laser fields is obtained as $\hbar\omega_{\text{max}}/\gamma m_e c^2 \sim \gamma^2\hbar\omega_L/m_e c^2 \sim 12\%$ in the case of $\gamma = 200$. Thus, one can expect that the energy loss by radiation emission affects largely the electron motion in such high intensity laser fields. Note that the relativistic factor can reach to larger values when electrons are accelerated for a long time without dephasing toward the direction of laser propagation by the Lorentz force ($\mathbf{v} \times \mathbf{B}$ force) as in vacuum or plasma channels.[35] In such a case, the relativistic factor scaled as $\gamma \sim a_0^2/2$ will result in higher energy radiation emissions.

The power of radiation from an accelerated electron is given by the Larmor formula, which can be represented in the relativistic form as[36]

$$P_{\text{rad}} = \frac{2}{3} r_e m_e c \gamma^6 \left[(\dot{\boldsymbol{\beta}})^2 - (\boldsymbol{\beta} \times \dot{\boldsymbol{\beta}})^2 \right], \tag{4}$$

where r_e is the classical electron radius, $\boldsymbol{\beta} = \mathbf{v}/c$, and the dot denotes the time derivative. Assuming quiver motion of electron by linearly polarized laser electric field, i.e., $d\mathbf{p}/dt = \omega_L m_e c \mathbf{a}/\gamma$ where $\boldsymbol{\beta} \parallel \dot{\boldsymbol{\beta}}$, we obtain

$$P_{\text{rad}} = \frac{2}{3} r_e \omega_L^2 m_e c \gamma^2 \mathbf{a}^2. \tag{5}$$

Here, we estimate the radiation power emitted from laser–matter interaction assuming overdense target with electron density n_e. In this case, the laser electric field causes oscillatory motion of electrons at the front surface of the target. The power density of radiation at the front surface is estimated by $p_{\text{rad}} = P_{\text{rad}} n_e$. Assuming laser wavelength $\lambda_L = 820$ nm and electron density $n_e = 10^{23}$ cm^{-3}, we obtain $p_{\text{rad}} = 1 \times 10^{25}$ W/cm^3 for $a_0 = 100$ and 2×10^{26} W/cm^3 for $a_0 = 200$, respectively. Since the strong interaction is expected in the width of skindepth λ_{skin} in the case of overdense target, the corresponding intensity of radiation is estimated by $I_{\text{rad}} = p_{\text{rad}} \lambda_{\text{skin}} = 2 \times 10^{20}$ W/cm^2 for $a_0 = 100$ and $I_{\text{rad}} = 4 \times 10^{21}$ W/cm^2 for $a_0 = 200$ when $\lambda_{\text{skin}} = 17\sqrt{\gamma}$ nm, i.e., the relativistic skin depth for $n_e = 10^{23}$ cm^{-3}. Comparing with the laser intensities for $a_0 = 100$ and 200, i.e., 2.0×10^{22} W/cm^2 and 8.1×10^{22} W/cm^2, respectively, we can see that the radiation intensity estimated in the above is not negligible, being 1%–5% of the incident laser energy. Due to such a high intensity radiation, the energy loss of electrons, i.e., the radiation damping, in the laser–matter interaction becomes important.

The estimated values for radiation power in the above can become even higher when ideal pre-plasmas are formed in the front region of the target material.[9] Furthermore, for the interaction of laser fields with cluster media, the radiation energy loss is expected to be more significant compared with materials with uniform structure, such as thin foils, since the interaction surface is larger including the area inside of the medium as is discussed in Sec. II.

IV. PIC SIMULATION INCLUDING THE RADIATION REACTION

In order to treat the damping effect of electron motion by the radiation emission in the PIC simulation, we consider the radiation reaction force $\mathbf{F}_{\text{rad}}$ as a friction in the equation of motion for electron as

$$\frac{d\mathbf{p}}{dt} = \mathbf{F}_L + \mathbf{F}_{\text{rad}}, \tag{6}$$

where $\mathbf{F}_L = -e(\mathbf{E} + \boldsymbol{\beta} \times \mathbf{B})$ is the Lorentz force.[32] Note that we can neglect the radiation friction to ions in the intensity regime assumed here due to the large mass ratio $m_i/m_e \sim 1800 Z \alpha$ where m_i is the ion mass, and $\alpha = 1$ and 2 for Hydrogen ($Z = 1$) and for species $Z \geq 2$, respectively. Namely, the relativistic factor for ions is m_e/m_i times smaller than that for electrons, and thus the radiation

power given by Eq. (4) for ions is considered to be negligibly small compared with that for electrons.

For the radiation reaction force, we here employ the Landau–Lifshitz formula given by[32]

$$\mathbf{F}_{\text{rad}} = \frac{2}{3} r_e \gamma \left(\frac{\partial}{\partial(ct)} + \boldsymbol{\beta} \cdot \nabla \right) \mathbf{F}_L$$
$$+ \frac{2}{3} r_e^2 [(\boldsymbol{\beta} \cdot \mathbf{E})\mathbf{E} + (\mathbf{E} + \boldsymbol{\beta} \times \mathbf{B}) \times \mathbf{B}]$$
$$- \frac{2}{3} r_e^2 \gamma^2 \boldsymbol{\beta} \left[(\mathbf{E} + \boldsymbol{\beta} \times \mathbf{B})^2 - (\boldsymbol{\beta} \cdot \mathbf{E})^2 \right], \tag{7}$$

which is the first-order formula derived from the energy conservation relation between the emitted radiation energy and the work done by the friction force $\mathbf{F}_{\text{rad}}$ with an assumption $F_L \gg F_{\text{rad}}$ in the rest frame of electron. Equation (7) is considered to be applicable below the laser intensity of quantum regime, in which the wavelength of laser field in the electron rest frame becomes small in the order of the Compton wavelength for single electron motion.[37,38] For the relativistic regime where $\gamma \gg 1$ is satisfied, the third term on the RHS of Eq. (7) which is in proportion to the highest order of the relativistic factor and the field amplitude, i.e., γ^2 and $\mathbf{E}^2$, becomes dominant.

Due to adding the force $\mathbf{F}_{\text{rad}}$ as a friction, the energy in the whole simulation system is damped. We regard the damped energy as the emitted radiation energy.

Note here that high energy radiations with the wavelength shorter than the simulation mesh size are not resolvable in the PIC simulation. From the estimated values for $\hbar \omega_{\text{max}}$ in Sec. III, we obtain the ratio between the corresponding wavelength λ_{max} and the mesh size of simulations we perform in this study, i.e., $L_{\text{mesh}} = 10$ nm, as $\lambda_{\text{max}}/L_{\text{mesh}} \sim 10^{-4} \ll 1$. Therefore, the dominant part of the high energy radiation emitted by accelerated electrons is not resolvable and thus not included in the calculation of fields in the simulation. This is equivalent to assuming that the emitted high energy radiations do not interact with plasma particles in the
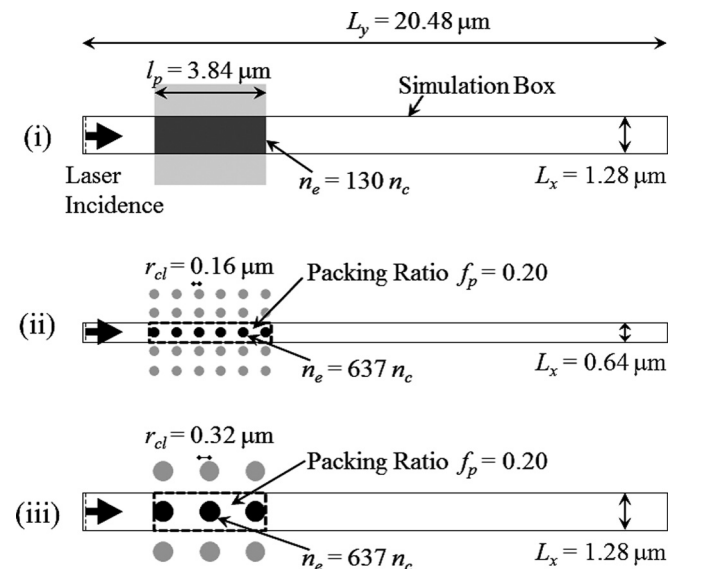

FIG. 3. Configuration of numerical simulation for cases (i)–(iii).

simulation system. This treatment is reasonable since the cross section for scattering of high energy photons by charged particles, i.e., the Compton scattering, is lower for higher photon energies being proportional to the inverse of the photon energy. A rigorous treatment of interaction between plasmas and the emitted high energy radiation are considered in Ref. 39 which becomes important in considering electron–positron pair production by the Bethe–Heitler process in high-Z material.

V. SIMULATION CONDITION

In order to consider the effects of clustered structure on the interaction with laser field in the radiation dominant regime, we execute 2D PIC simulations by assuming three configurations shown in Fig. 3, i.e., (i) uniform plasma and cluster media composed of (ii) small clusters with radius $r_{cl} = 160$ nm and (iii) large clusters with radius $r_{cl} = 320$ nm, where all the media (i)–(iii) have the same total mass. The simulations are performed using the EPIC code in which we included the radiation reaction force as described in Sec. IV.

The simulation boxes set for cases (i)–(iii) are shown in Fig. 3. We set the periodic boundary condition in the x direction so that the plasma or clusters are distributed infinitely in the x direction as shown outside of the simulation box in Fig. 3 in gray. On the other hand, the boundary condition for the y direction is outgoing, so that particles and fields that reach to the $y = 0$ or $y = L_y$ boundary go out of the simulation system. Here, the size of the simulation box is $L_y = 20.48\ \mu$m in the y direction and $L_x = 1.28\ \mu$m for cases (i) and (iii), and $L_x = 0.64\ \mu$m for case (ii), in the x direction. The mesh size is $L_{mesh} = 10$ nm in both x and y directions.

We assume an antenna located at $y = 0.02\ \mu$m that excites a p-polarized laser pulse with the wavelength $\lambda_L = 820$ nm. The laser field is uniform in the x direction while having the Gaussian time profile with duration $2\tau = 40$ fs where τ corresponds to the half width of the Gaussian pulse function which is proportional to $\exp(-t^2/\tau^2)$. The peak amplitude of the laser field is given by $\hat{a}_0 = 100$ or 200. Note that the situations considered here are essentially one dimensional, since we assume the transversely uniform laser field together with the periodic boundary in x.

Media (i)–(iii) consist of fully ionized carbon plasmas ($Z = 6$). The ion density of clusters in cases (ii) and (iii) is assumed to be the diamond density, i.e., $n_i = 1.76 \times 10^{23}$ cm^{-3}. The electron density for (ii) and (iii) is then given by $n_e = Z n_i = 637\ n_c$. Clusters are modeled by uniform plasma columns where the cluster sizes are determined on the basis of the discussions given in Sec. II. Note that $r_{cl} = 160$ nm and 320 nm in cases (ii) and (iii) are the radii which result in $|e\phi_{cl}^{2D}|/\epsilon_k < 1$ and $|e\phi_{cl}^{2D}|/\epsilon_k > 1$, respectively, for $a_0 = 100$ in Fig. 2. The packing ratio is given by $f_p = N_{cl}\pi r_{cl}^2/S = 0.20$ where N_{cl} is the number of clusters in the simulation box and the background area S is shown by the dashed line in Fig. 3. The clusters are distributed regularly where the distance between the cluster surfaces is almost the same as the cluster diameter. The ion and electron densities for uniform plasma (i) is set to be the averaged density in the cluster media, i.e., $n_{av} = f_p n_e = 130\ n_c$.

VI. INTERACTION WITH $\hat{a}_0 = 100$ LASER FIELD

A. Energy evolution in each medium

In this section, we consider the interaction with laser peak amplitude $\hat{a}_0 = 100$. In this case, the assumed average density $n_{av} = 130 n_c$ is overdense even when we consider the relativistic effect, i.e., the relativistic cutoff density $\gamma n_c \sim \hat{a}_0 n_c/\sqrt{2} = 71 n_c$ is still smaller than n_{av}.

First, we study the energy partition among electrons, ions, and radiations during the interactions by presenting the time evolution of energy densities of electrons ε_e, ions ε_i, and field ε_f in the simulation system, and that of radiation energy loss ε_{rad} calculated from the time integration of the corresponding power $\mathbf{v} \cdot \mathbf{F}_{rad}$. Here, all the energy densities are averaged by the total volume of the system V. The explicit definitions are given in Appendix A.

The above energy densities are shown in Figs. 4(i-a), 4(ii-a), and 4(iii-a). Here, the values are normalized by the total energy input during the time $t = 0$ to t_{final} by the laser into the simulation box, i.e., ε_{in}, which is also divided by the total volume of the system. Here, $t_{final} = 200$ fs corresponds to the final time of the simulation. The normalized values are represented with tilde, e.g., $\tilde{\varepsilon}_e(t) = \varepsilon_e(t)/\varepsilon_{in}(t_{final})$ is the normalized electron energy density. Note that in this notation, $\tilde{\varepsilon}_{in}(t_{final}) = 1$. We also plot the total absorption energy $\tilde{\varepsilon}_{abs} = \tilde{\varepsilon}_e + \tilde{\varepsilon}_i$ in Figs. 4(i-a)–4(iii-a). We note that the energy conservation relation can be represented as $\tilde{\varepsilon}_e(t) + \tilde{\varepsilon}_i(t) + \tilde{\varepsilon}_f(t) + \tilde{\varepsilon}_{Poy}(t) + \tilde{\varepsilon}_{rad}(t) = \tilde{\varepsilon}_{in}(t)$. Here, $\tilde{\varepsilon}_{Poy}$, which is not shown in Fig. 4, is the normalized Poynting energy denoting the energy of reflected and/or transmitted wave that has gone out from the y-boundaries of the simulation box up to the time t. The conservation relation is confirmed to be well satisfied as shown by Fig. 14 including $\tilde{\varepsilon}_{Poy}$ in Appendix A.

We see from Figs. 4(i-a)–4(iii-a) that the field energy (black solid line) increases initially, and then, from around $t = 50$ fs, the absorption energy (blue bold line) begins to increase. Note that the laser pulse peak reaches to the front surface position $y = 2.56\ \mu$m at $t = 62$ fs in the case of vacuum. Around this pulse peak time, the energy absorption by electrons becomes the largest by which the electron energy absorption rate reaches to $\tilde{\varepsilon}_e \sim 0.3$ for the case of uniform plasma (i) and $\tilde{\varepsilon}_e > 0.4$ for cluster media (ii) and (iii). After $t = 80$ fs, as the laser input is almost finished as seen from the saturation of $\tilde{\varepsilon}_{in}$, the electron energy begins to decrease while the ion energy (blue dashed line) increases by the same gradient. As a result, the total particle absorption energy $\tilde{\varepsilon}_{abs}$ remains constant after the time. This indicates that the electron energy is converted to the ion energy due to ion acceleration by the electrostatic field created by the expanding electrons.

The radiation energy $\tilde{\varepsilon}_{rad}$ shown by the red dashed-dotted line increases during the peak interaction time $t = 50 - 80$ fs and remains constant after the time for all the cases. This indicates that the radiation loss takes place dominantly at the time when electrons are interacting with the laser field of large amplitude. The radiation energy loss rates at the final time, $\tilde{\varepsilon}_{rad}(t_{final})$, are obtained as 1.4%, 8.3%, and 8.9% for cases (i)–(iii), respectively.
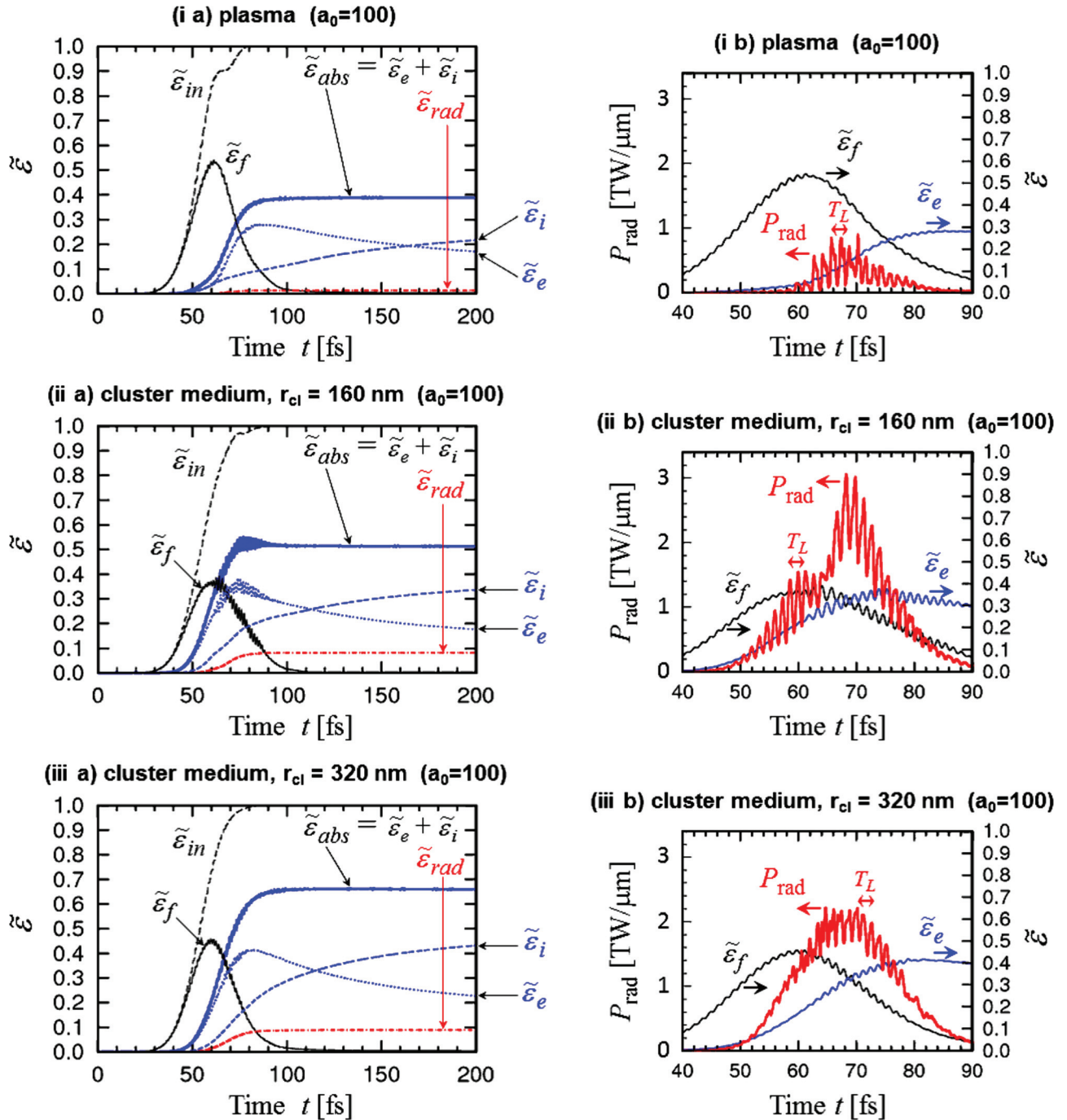
FIG. 4. ((i-a)–(iii-a), left) Time evolution of energy densities averaged by volume for field $\tilde{\varepsilon}_f$ (black solid line), electron $\tilde{\varepsilon}_e$ (blue dotted), ion $\tilde{\varepsilon}_i$ (blue dashed), absorption $\tilde{\varepsilon}_{abs}$ (blue solid), and radiation $\tilde{\varepsilon}_{rad}$ (red dashed-dotted), which are normalized by the final value of the input energy ε_{in} ($t = 200$ fs), for media (i)–(iii). ((i-b)–(iii-b), right) Radiation power (red bold line) during $t = 40$–90 fs for the same simulations as the left side figures for each medium. Energy densities for field $\tilde{\varepsilon}_f$ (black) and electron $\tilde{\varepsilon}_e$ (blue), which are the same as those in the left side (a), are shown for reference. For all results, the assumed laser peak intensity is $\hat{a}_0 = 100$.

In the right side in Fig. 4, i.e., (i-b), (ii-b), and (iii-b), $\tilde{\varepsilon}_f$ and $\tilde{\varepsilon}_e$ in $t = 40$–90 fs are closed up. In addition, we show the power of radiation P_{rad} in the same figure by red bold line. Note that for case (ii), we doubled the value of P_{rad} obtained in the simulation in order to compare it with the other cases, since the size of the simulation box for case (ii) is half of those in cases (i) and (iii). In the radiation power P_{rad}, coherent radiation emissions with period $T_L/2$, where $T_L = 2\pi/\omega_L$ is the laser period, are seen in all the cases (i)–(iii). One can see that the oscillations in P_{rad} synchronize with those in the

field and electron energies, $\tilde{\varepsilon}_f$ and $\tilde{\varepsilon}_e$. This indicates that the electrons oscillate in the direct interaction with the laser electric field whose strength changes in the period of $T_L/2$, and due to such strong accelerations, the electrons emit high energy radiations with the same period $T_L/2$.

Here, the minimum value in the oscillatory part of P_{rad} does not reach to zero specifically in the case of cluster media (ii) and (iii). The remained incoherent component represents radiations by quivering motion of electrons by laser field at positions of different phase, and also by accelerated motions

by the Coulomb field from cluster surfaces. On the other hand, the dominance of oscillatory component of P_{rad} in case (i) indicates that the most part of radiation is emitted from the coherent oscillatory motion of electrons by laser electric field at the front surface of the plasma distribution. We find that the enhancement of radiation energy $\tilde{\varepsilon}_{rad}$ in the cluster media which we have seen in Figs. 4(i-a)–4(iii-a) resulted mainly from the increase of the incoherent part of P_{rad}.

Here, amplitude of the coherent oscillatory part of P_{rad} in case (ii), whose maximum value reaches to $1.2\,\text{TW}/\mu\text{m}$, is about twice larger than that in case (iii). This is considered to be resulted from the twice larger surface in case (ii) at the same position in y where electrons move with the same phase coherently. Namely, the numbers of clusters distributed in the x direction in length $1.28\,\mu\text{m}$ are 2 and 1 for cases (ii) and (iii), respectively, and thus, the points on cluster surface that are positioned at the same coordinate in y are doubled in case (ii), which enhances the coherent part of P_{rad}.

The radiation power reaches to $3\,\text{TW}/\mu\text{m}$ instantaneously in case (ii), which is the largest among cases (i)–(iii). If we assume that the radiation takes place uniformly in a laser spot area S_{spot} of $5\,\mu\text{m}$ diameter for instance, the corresponding radiation power for the cluster medium (ii) becomes 59 TW.

Note that, in the radiation power for case (ii), two peak periods with large oscillations around $t = 60$ fs and $t = 70$ fs are seen. It is confirmed that these peaking times of P_{rad} correspond to the times when the laser field is passing between clusters that have not yet dissolved to be uniform. Therefore, the first and second peak periods of P_{rad} correspond to the times when the laser field interacts with the surface electrons at the first and second clusters, respectively.

B. Two dimensional spatial distribution of radiation energy loss

In Subsection VI A, we found that cluster media exhibit higher radiation rates compared with the uniform plasma. We here compare the interaction dynamics of each medium, which results in the difference of the radiation rates.

In Fig. 5, we show the two-dimensional distributions of field, electrons, and radiation energy loss for each medium. All the plots in Fig. 5 are for the instant time $t = 70.1$ fs around which the total energy in the system becomes the largest. The upper figures (a), i.e., (i-a), (ii-a), and (iii-a), are one-dimensional plots at the center of the system, $x = L_x/2$, for charge density of electrons n_e (black) and ions Zn_i (blue) for media (i)–(iii). The upper two contours (b) and (c) represent the 2D distributions of electric field E_x ((i-b), (ii-b), and (iii-b)) and electron density n_e ((i-c), (ii-c), and (iii-c)), respectively, where they are also normalized by the peak laser amplitude E_0 and cutoff density n_c, respectively. In the color bar for electron density n_e, the colors are separated rigidly so that the relation with relativistic cutoff density γn_c can be seen clearly. Namely, with the assumption of $\gamma = \sqrt{1 + a_0^2/2}$, the values on the color bar 35, 71, 106, and 141 indicate the relativistic factor γ for $a_0 = 50, 100, 150$ and 200, respectively. Therefore, $n_e/n_c = 35, 71, 106$, and 141 correspond to the relativistic cutoff densities for the laser
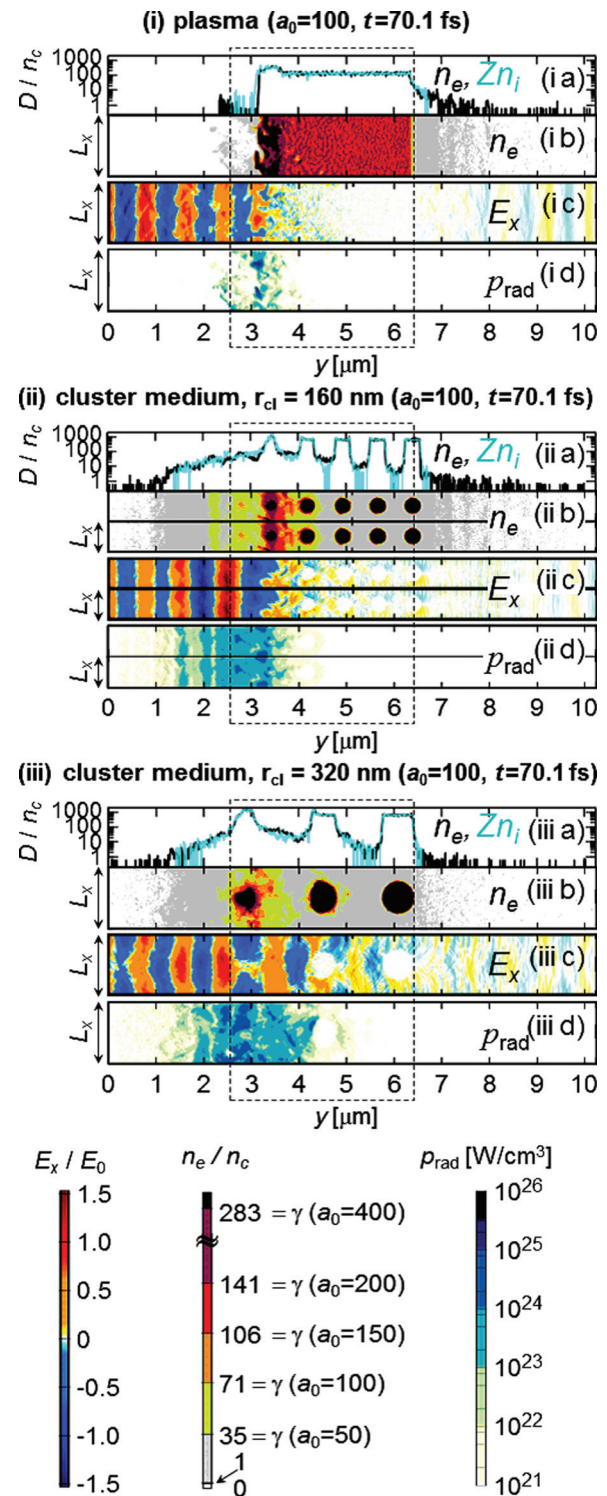

FIG. 5. One dimensional snap shots of (a) charge density of electron n_e (black) and ion Zn_i (blue) and two dimensional contours of (b) electron density n_e, (c) electric field E_x, and (d) radiation energy density ε_{rad} at $t = 70.1$ fs for the case of $\hat{a}_0 = 100$.

field amplitudes $a_0 = 50, 100, 150$, and 200, respectively. The dashed lines in the figures indicate the initial distribution area for each medium.

In the lowest contour, we present the power density of radiation p_{rad} that is obtained from the work done by the radiation reaction force $\mathbf{F}_{rad}$ to electrons in each simulation cell. The detail of the calculation is presented in Appendix B.

First, in the case of plasma (i), the high density region of $n_e/n_c > 141$ (dark-red and black) is formed at the front surface of the plasma being pushed by the laser field. The radiation loss for case (i) is seen at the peripheral of the front surface, i.e., $2.6\,\mu m \leq y \leq 3.8\,\mu m$, where the electrons interact with the incident laser field. The radiation power density obtained for this case (i) is typically in the order of $10^{23}\,W/cm^3$.

Second, for the cluster medium with small clusters (ii), the first cluster has just been dissolved at this time. From Fig. 5(ii-b), it is seen that the electrons from the first cluster are pushed by the laser field to the second cluster position and make a one-dimensional wall structure with $141 < n_e/n_c < 283$, by which the laser field coming after the time is reflected as in (ii-c). As seen from (ii-b), electrons are distributing in regime $y = 2.3 - 4.5\,\mu m$ with density $35 < n_e/n_c < 71$ (green) that is high but underdense for the field amplitude $a_0 = 100$. Owing to such a cluster expansion during the interaction, the larger number of electrons can interact directly with the laser field compared with case (i). As a result, the radiation loss shown in (ii-d) distributes in wider area than that in (i).

Third, for the cluster medium with large clusters (iii), the electron core of the first cluster still remains with density $n_e/n_c > 283$ as seen in (iii-b). Here, since the inter-cluster distance in case (iii) is twice larger than that in case (ii), the region with $n_e/n_c < 71$ which is relativistically underdense for the laser field amplitude of $a_0 = 100$ still exists in case (iii) between clusters with respect to the x direction. The laser field can then penetrate into the medium as seen in (iii-c). The radiation loss distributes in the area $1.8\,\mu m \leq y \leq 4.4\,\mu m$ beyond the position of the remaining first cluster. A high radiation power density in the order of $10^{24}\,W/cm^3$ can be seen also at the second cluster surface.

From Figs. 5(i)–5(iii), it is found that the high power density of radiation loss distributes in the area where electrons with near-critical density and strong laser field in the level of $E_x/E_0 \sim 1$ are overlapped. Namely, the wider distribution of the radiation loss in cluster media (ii) and (iii) than in case (i) reflects the wider expansions of electrons to the front side for case (ii), and both front side and inside for case (iii), respectively, which are shown in green and gray colors ($1 \leq n_e/n_c \leq 71$) in Figs. 5(ii-d) and 5(iii-d).

Here, the electron expansion to the front side in the cluster media can be understood as follows. In the case of uniform plasma distribution (i), the front surface is pushed uniformly by the laser field. On the other hand, in the case of cluster media (ii) and (iii), the laser fields tend to penetrate through the low-density region between clusters, and therefore, the pressure at the front of the each cluster are diminished compared with the uniform case (i). A large number of electrons from clusters can then expand not only to the rear but also to the front direction.

VII. INTERACTION WITH $\hat{a}_0 = 200$ LASER FIELD

A. Energy evolution in each medium

Next, we consider the interaction with higher laser peak amplitude $\hat{a}_0 = 200$. In this case, the assumed average density $n_{av} = 130 n_c$ is underdense considering the relativistic

effect. Namely, the cutoff density is estimated to be $\gamma n_c \sim \hat{a}_0 n_c / \sqrt{2} = 141 n_c$ which is a little higher than n_{av}.

We first show the time evolution of the averaged energy densities in Fig. 6. The definition of each energy is the same as that in Fig. 4. We notice in the left side of Fig. 6 for the cluster media (ii) and (iii), i.e., (ii-a) and (iii-a), that the final value of the absorption energy density $\tilde{\varepsilon}_{abs}$ ($t_{final} = 200$ fs) decreases largely compared with that in the case of $\hat{a}_0 = 100$. Instead, the radiation energy density $\tilde{\varepsilon}_{rad}$ is found to increase significantly compared with the case of $\hat{a}_0 = 100$. As a result, the absorption rate $\tilde{\varepsilon}_{abs}$ in cluster media (ii) and (iii) is found to become almost the same value as that for the uniform plasma (i) in the current case $\hat{a}_0 = 200$. The ratio of energy depositions to electrons $\tilde{\varepsilon}_e$ and ions $\tilde{\varepsilon}_i$ are also the same among cases (i)–(iii).

The radiation energy density $\tilde{\varepsilon}_{rad}$ evolves during the time $t = 50 - 80$ fs with the increase of $\tilde{\varepsilon}_{abs}$ in a similar manner with the case of $\hat{a}_0 = 100$. Here, $\tilde{\varepsilon}_{rad}$ in case (iii), which takes the highest value among cases (i)–(iii), reaches to the value near to that of the absorption rate $\tilde{\varepsilon}_{abs}$. The final radiation loss rates $\tilde{\varepsilon}_{rad}$ (t_{final}) are obtained as 13%, 31%, and 36% for cases (i)–(iii), respectively. Therefore, the relative relation that the radiation rates in cluster media are larger than the uniform plasma (i) is sustained as the laser field amplitude is increased from $\hat{a}_0 = 100$ to 200.

In the right side in Fig. 6, i.e., (i-b)–(iii-b), we show the radiation power P_{rad} and the normalized energy densities for field $\tilde{\varepsilon}_f$ and electrons $\tilde{\varepsilon}_e$ for $t = 40$–90 fs.

As same as in the case of $\hat{a}_0 = 100$, we see that the coherent oscillatory component of P_{rad} dominates in the case of uniform plasma (i), whereas the incoherent component is large in the cluster media (ii) and (iii). For cases (i) and (ii), the amplitude of the coherent oscillation in P_{rad} in the current case $\hat{a}_0 = 200$ is about 17 and 15 times larger, respectively, compared with those for $\hat{a}_0 = 100$. The above increase factor, which is near to the value $16(=2^4)$, is reasonable, since the radiation power given by Eq. (5) shows the dependence on $\gamma^2 a_0^2 \sim a_0^4$, and the ratio of $\hat{a}_0$ is currently $200/100 = 2$. As for case (iii), the ratio of maximum amplitude of the coherent oscillation in P_{rad} between cases $\hat{a}_0 = 100$ and 200 is more than 20. This is due to that the coherent radiation emission is contributed not only from the first cluster which is located at the most front side, but also from the second cluster whose center is initially located at a distance of $1.94\lambda_L$, i.e., about twice the laser wavelength, from that of the first cluster.

Different from the case of $\hat{a}_0 = 100$, the amplitude of the coherent oscillatory part of P_{rad} in case (ii) shows similar value to the other cases (i) and (iii). This denotes that the clustered structure in case (ii) is dissolved to be uniform in a short time during the interaction with the laser field of $\hat{a}_0 = 200$. Note that the short-time expansion can also be expected from Fig. 2 discussed in Sec. II where the small cluster $r_{cl} = 160$ nm satisfies $|e\phi_{cl}^{2D}|/\epsilon_k \ll 1$ for $a_0 = 200$ even when all the electrons are expelled from the cluster to be $r_0 = 0$. Hence, the uniform distribution can be easily formed in case (ii) for the case of $\hat{a}_0 = 200$, and the property that the cluster medium (ii) has larger interaction surface disappears in a short time.
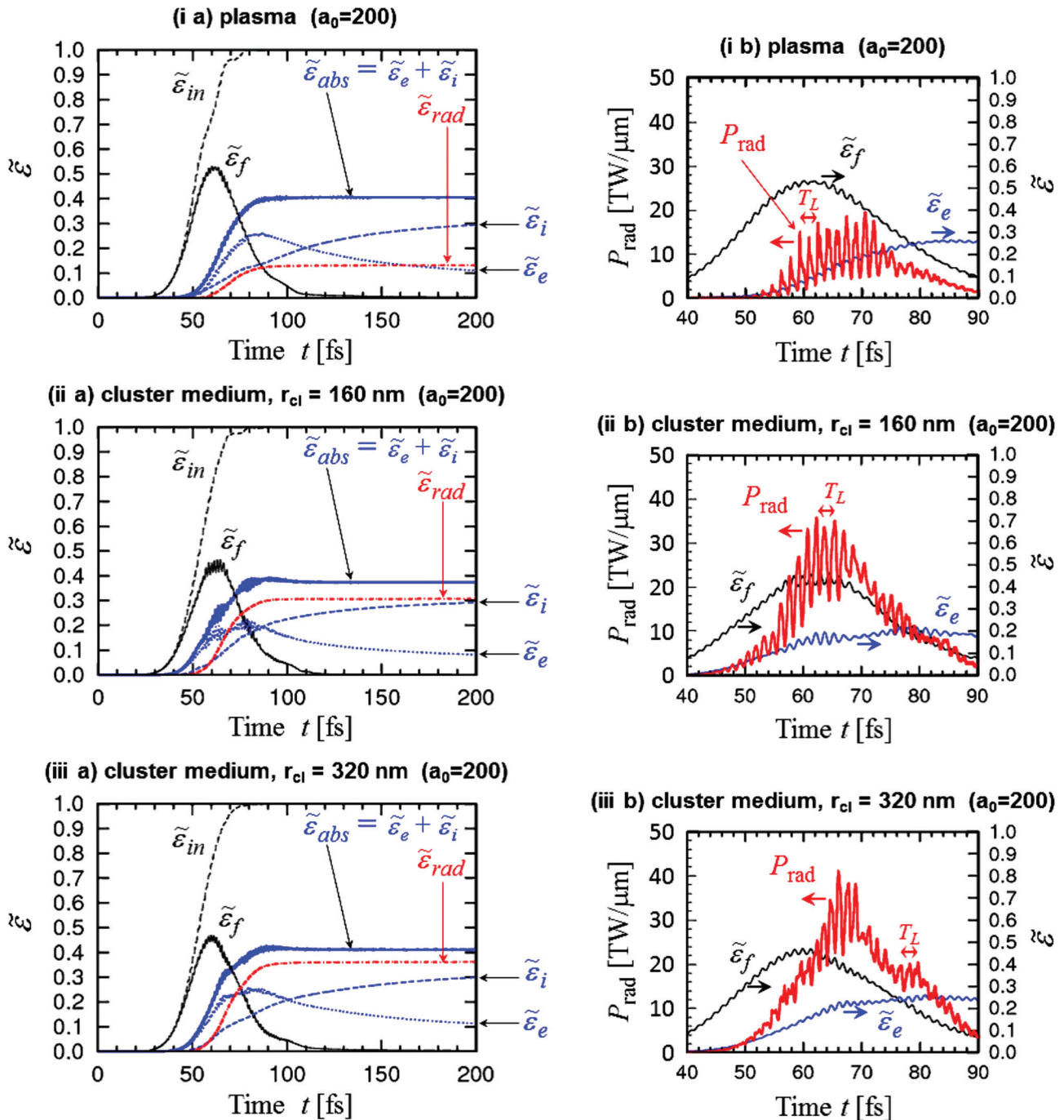
FIG. 6. ((i-a)–(iii-a), left) Time evolution of energy densities averaged by volume for field $\tilde{\varepsilon}_f$ (black solid line), electron $\tilde{\varepsilon}_e$ (blue dotted), ion $\tilde{\varepsilon}_i$ (blue dashed), absorption $\tilde{\varepsilon}_{abs}$ (blue solid), and radiation $\tilde{\varepsilon}_{rad}$ (red dashed-dotted), which are normalized by the final value of the input energy ε_{in} ($t = 200$ fs), for media (i)–(iii). ((i-b)–(iii-b), right) Radiation power (red bold line) during $t = 40$–90 fs for the same simulations as the left side figures for each medium. Energy densities for field $\tilde{\varepsilon}_f$ (black) and electron $\tilde{\varepsilon}_e$ (blue), which are the same as those in the left side (a), are shown for reference. For all results, the assumed laser peak intensity is $\hat{a}_0 = 200$.

The radiation power reaches to $40\,\mathrm{TW}/\mu m$ instantaneously in case (iii), which is the largest among cases (i)–(iii). If we assume a laser spot area S_{spot} of $5\,\mu m$ diameter as same as in Sec. VI A, the corresponding radiation power for the cluster medium (iii) becomes 0.78 PW.

B. Two dimensional spatial distribution of radiation energy loss

Next, we investigate the interaction by using two-dimensional figures (Fig. 7). All the plots and contours in Fig. 7 are for the instant time $t = 70.1$ fs as same as in Fig. 5.

First, in the case of plasma (i), the front surface is pushed by the radiation pressure of the laser field for a distance about $1\,\mu m$ from the initial front position as seen in (i-b), and as a result, the high density region with $n_e/n_c > 141$ (dark-red and black) is made at the surface. Therefore, despite that the original plasma density $n_e = 130n_c$ is underdense for the field amplitude $a_0 = 200$, the laser field cannot propagate exceeding the high density surface with $n_e/n_c > 141$ as seen in Fig. 7(i-c). At the front of the interaction surface, high intensity radiation losses that reach to the level of $10^{26}\,\mathrm{W/cm^3}$ are obtained.
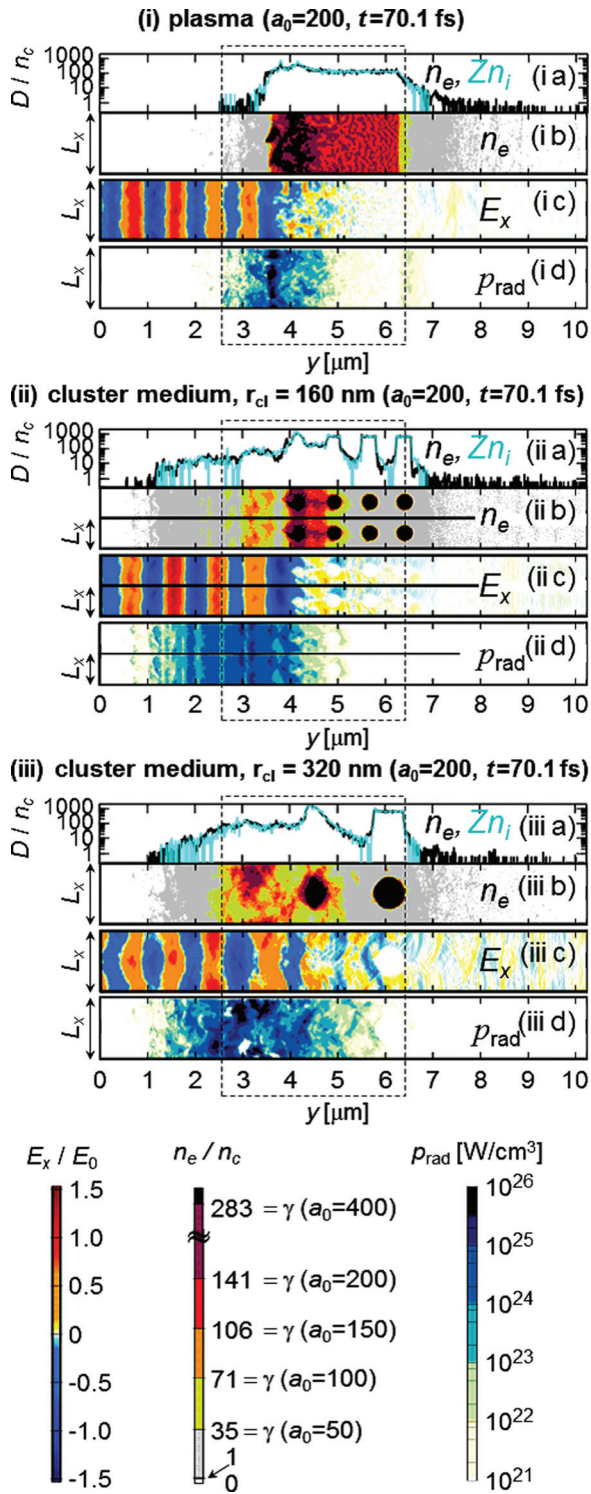
FIG. 7. One dimensional snap shots of (a) charge density of electron n_e (black) and ion Zn_i (blue) and two dimensional contours of (b) electron density n_e, (c) electric field E_x, and (d) radiation energy density ε_{rad} at $t = 70.1$ fs for the case of $\hat{a}_0 = 200$.

Second, for the cluster medium (ii), the electrons from the first and second clusters are pushed by the laser field toward the position of the third cluster and make a high density wall with $n_e/n_c > 141$ which is relativistically overdense for the field amplitude $a_0 = 200$. The laser field reaches to the front surface of the third cluster, exceeding the relativistically underdense region of $35 \leq n_e/n_c \leq 106$ (green and

orange). Although both cases (i) and (ii) produce the high density wall structure one-dimensionally, by which the laser field is reflected, the difference of the initial structure between cases (i) and (ii) can be seen clearly in (ii-d) as the wider distribution of intense radiation loss in the front side of the medium in case (ii). Namely, the radiation loss in the order of 10^{23-24} W/cm^3 seen from $y = 1.7\,\mu m$ to $2.6\,\mu m$ in (ii-d) is not seen in case (i). This coincides with the wider expansion of the electrons to the $-y$ direction in the cluster medium, as is discussed for $\hat{a}_0 = 100$ in Sec. VI B. Such a wider distribution of radiation results in the larger value of the incoherent part of P_{rad} shown in Fig. 6(ii-b).

Third, for the cluster medium with larger clusters (iii), it is seen from Fig. 7(iii-b) that the electrons from the first and second clusters form a high density region with $71 \leq n_e/n_c \leq 141$ (orange and red), which is high but underdense for the field amplitude $a_0 = 200$, around $y = 3 - 4\,\mu m$. Such a wide distribution of near-critical density is seen only for case (iii), which results in the high energy absorption and radiation rates in (iii) shown in Fig. 6. Note that no electron core is remained at the original first cluster position, i.e., $y = 2.6$–3.2 μm, in Fig. 7(iii-b) for the current case $\hat{a}_0 = 200$ as is expected in the discussion for Fig. 2 in Sec. II. From Fig. 7(iii-c), it is seen that the laser field penetrates through the low density region between clusters in the x direction and reaches to the rear side with a small amplitude. In this time $t = 70.1$ fs, intense radiation losses that reach to the level of 10^{25} W/cm^3 are obtained at the peripheral of the first cluster and also at the front surface of the second cluster as shown in (iii-d). Such an intense radiation indicates that the number of electrons that emit high energy radiation is increased in case (iii) compared with cases (i) and (ii).

VIII. RATES OF ENERGY CONVERSION

Here, we summarize the variation of energy conversion rates from laser to particles and high energy radiations at the final time $t_{final} = 200$ fs with $\hat{a}_0 = 100$, 150, and 200 in Fig. 8. The upper figure, Fig. 8(a), represents the absorption rate $\tilde{\varepsilon}_e + \tilde{\varepsilon}_i$ obtained in the simulations without radiation reaction. The triangle, circle, and square points represent the rates for cases (i), (ii), and (iii), respectively. On the other hand, in the lower figure, Fig. 8(b), the absorption and radiation rates obtained in the simulation with radiation reaction are shown in blue and red, respectively, on the left side. On the right side, the sum of absorption and radiation rates $\tilde{\varepsilon}_e + \tilde{\varepsilon}_i + \tilde{\varepsilon}_{rad}$ for simulations with radiation reaction is shown.

Note that by observing the Poynting energy at the y boundaries, we confirmed that the transmission rate of the field to the rear boundary is less than 2% for all the cases. Therefore, the energy which is not absorbed or lost as the radiation emission corresponds to the reflected Poynting energy that goes out of the system from the $y = 0$ boundary.

In the case without radiation reaction (Fig. 8(a)), the absorption rate for the uniform plasma (i) shown by blue triangles increases as the laser field amplitude $\hat{a}_0$ increases. This is due to the relativistic penetration of the laser field for larger $\hat{a}_0$. When the radiation reaction is taken into account, the absorption rate for case (i) saturates even $\hat{a}_0$ increases as seen in the left side of Fig. 8(b). Instead, the energy
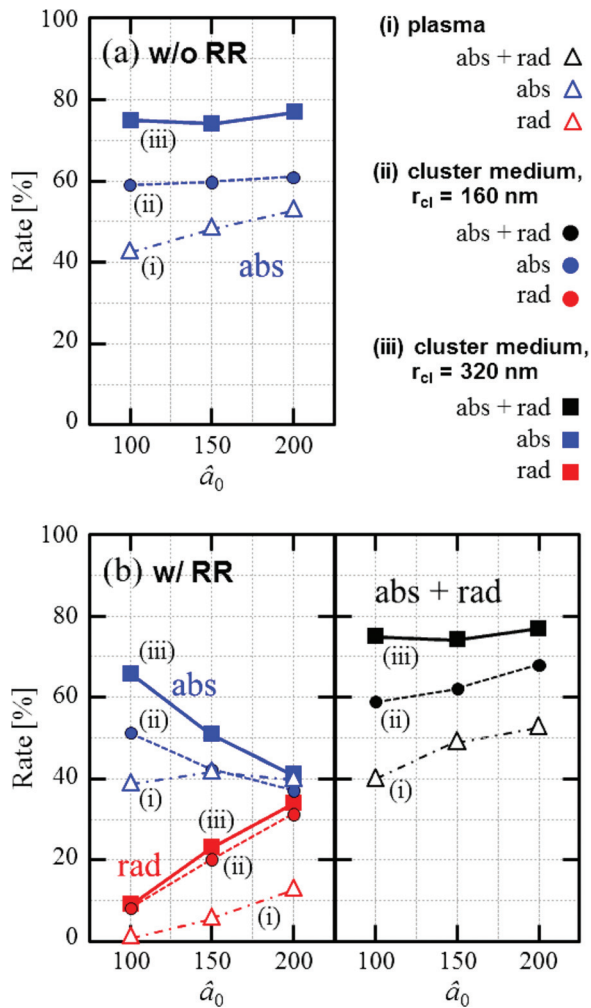
FIG. 8. Dependence of absorption and radiation rates on the peak normalized amplitude of the incident laser field $\hat{a}_0$. (a) Absorption rates obtained in the simulations without radiation reaction are shown by blue triangles, circles, and squares for media (i) uniform plasma, (ii) cluster medium with cluster radius $r_{cl} = 160$ nm, and (iii) cluster medium with $r_{cl} = 320$ nm, respectively. (b) Results for the cases with radiation reaction. On the left side panel, absorption (blue) and radiation (red) rates are plotted for each medium. On the right side panel, the sum of absorption and radiation rates is shown in black for each medium (i)–(iii).

conversion to the radiation (red triangles) increases with almost the same gradient as that for the absorption rate in the case without radiation reaction. As a result, the absorption rate without radiation reaction and the sum of absorption and radiation rates (black triangle on the right side of Fig. 8(b)) exhibit the same variation with respect to $\hat{a}_0$.

In the case of cluster medium with large clusters (iii), all the rates shown in Fig. 8 by square points exhibit the largest value among the three cases (i)–(iii) for each $\hat{a}_0$. We note that the rates for cluster medium with small clusters (ii) exhibit the intermediate values between those for cases (i) and (iii). This is reasonable since the configuration of the cluster medium (ii) shown in Fig. 3 is taken to be the intermediate structure between cases (i) and (iii).

For the interaction without radiation reaction in (iii), the absorption rate represented by blue squares in Fig. 8(a) reaches to around 75% and exhibits little variation for different $\hat{a}_0$, i.e., the rate increases only 3% from the case of $\hat{a}_0 = 100$ to that of

$\hat{a}_0 = 200$. By the inclusion of radiation reaction, the absorption rate for (iii) is reduced especially for large $\hat{a}_0$ as shown by blue squares on the left side of Fig. 8(b). For instance, for $\hat{a}_0 = 200$, the absorption rate for (iii) is reduced by the radiation damping to the half value, i.e., from 80% to 40%. The latter is the same level as the absorption rates in the case of plasma (i) and also in (ii) with radiation reaction. Namely, for $\hat{a}_0 = 200$, the absorption rates for all the cases (i)–(iii) decreased to around 40% by the radiation damping. However, we find that the radiation rates, which are shown in red, for cluster media increase with $\hat{a}_0$ with almost the same gradient as the decrease of the absorption rate for (iii).

As a result, for case (iii), the sums of absorption and radiation rates in the right side of Fig. 8(b) show almost the same values as the absorption rates without radiation reaction shown in Fig. 8(a). For cluster medium (ii), due to the smaller gradient of the decrease of the absorption rate (blue circles) compared with that in the increase of the radiation rate (red circles), the sum of absorption and radiation rates increases for $\hat{a}_0 = 200$, which is a different behavior from the absorption rate without radiation reaction.

The above results denote that the conversion ratio between particle and radiation differs depending on the internal structure of the medium. We conclude that the cluster media assumed here provide effective conversions to high energy radiations.

IX. ELECTRON TRAJECTORY IN THE INTERACTION WITH $\hat{a}_0 = 200$ LASER FIELD

As summarized in Fig. 8, we have so far seen large radiation energy losses in the cluster media. Since the radiation reaction acts on electrons, the effect can be seen directly in the electron trajectories. To see it, we compare the electron trajectories obtained in the simulations without and with radiation reaction for cases (i)–(iii) in Figs. 9–11, respectively. By the colors of the trajectories, we also show the relativistic factor of the electrons. The dashed lines in the figures represent the initial surfaces of plasma or clusters. The black dots on the trajectories correspond to the positions of the electron at $t = 0$ fs and 70.1 fs. Since we employed the periodic condition for the x boundary, we connected the trajectories coming to the position $x = x_\alpha$ across the boundary $x = L_x$ for n times to $x = x_\alpha + nL_x$, and vice versa for $x < 0$.

First, we show trajectory of an electron in the uniform plasma (i) in Fig. 9. In this case, the trajectory obtained from simulation with radiation reaction shown in the lower figure shows basically the same behavior as that for the case without radiation reaction shown in the upper figure. The electron moves from the initial position to the direction of the front surface as the return current with a slow velocity. At the front surface of the plasma, the electron interacts with the laser field and changes its direction to the $+y$ direction due to the $\mathbf{v} \times \mathbf{B}$ force. After the time, the electron moves toward the rear side surface in a ballistic trajectory with a slow velocity of $\gamma \sim 30$ in the case without radiation reaction and that of smaller energy $\gamma \sim 6$ in the case with radiation reaction. At the rear surface, the electron again changes its direction to the $-y$ direction being dragged by the sheath field of

(i) plasma ($a_0 = 200$)

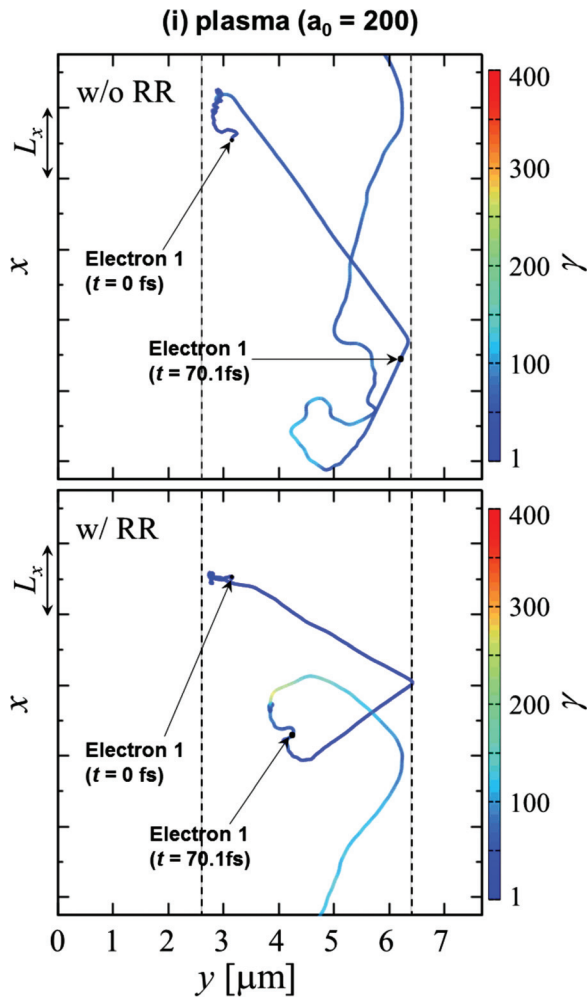## (ii) cluster medium, $r_{cl} = 160$ nm ($a_0 = 200$)

FIG. 9. Electron trajectory in uniform plasma (i) for $\hat{a}_0 = 200$ without (upper) and with (lower) radiation reaction. Dashed lines represent the initial surface of plasma.
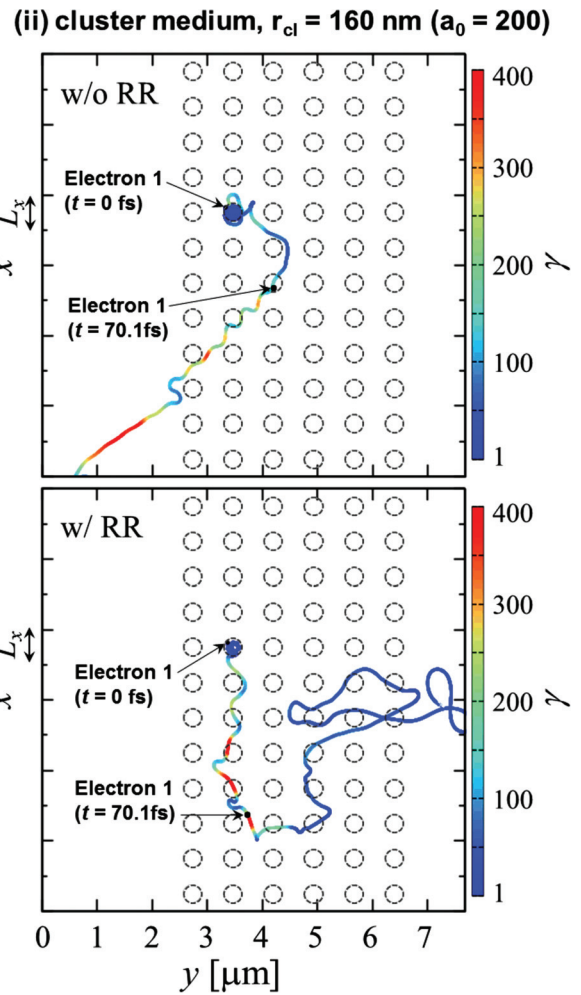
FIG. 10. Electron trajectory in cluster medium (ii) for $\hat{a}_0 = 200$ without (upper) and with (lower) radiation reaction. Circles with dashed line represent the initial position of clusters.

the plasma. Interaction with the laser field again takes place at around $y = 4\,\mu$m, which roughly corresponds to the position of the interaction front at time $t = 70.1$ fs as is seen in Figs. 7(i-b) and 7(i-c). Such a ballistic trajectory with no rapid change of the energy will not contribute to high energy radiation emissions.

Second, in Fig. 10, trajectory of an electron from the second cluster is shown. In the case without radiation reaction, the electron that has left the cluster changes its direction around the third cluster, moves to the direction of the front surface, and goes away from the medium. After $t = 70.1$ fs, the electron oscillates due to the force from the laser electric field whose pulse front is coming to $y = 4\,\mu$m at $t = 70.1$ fs as shown in Fig. 7(ii-c). Such a quiver motion with a large momentum to the counter direction to the laser field is expected to suffer from a large radiation friction, since the power of radiation from an accelerated charge, which is in proportion to the acceleration frequency ω_L as in Eq. (5), becomes larger when blue shift of the frequency takes place due to the counter propagation of the charge and the field.

We see in the lower figure in Fig. 10 that the electron loses its momentum of the $-y$ direction around the surface of the medium due to the radiation damping, and consequently the electron is pushed back into the medium after excursion at

the peripheral of the second cluster. We note that during the excursion, the second cluster core still remains and the ion core disappears to be uniform at just after the time $t = 70.1$ fs. The electron trajectory for case (ii) in the lower figure in Fig. 10 represents that the electron stays around the second cluster core and interacts with the laser field and charge separation field until the clustered structure becomes uniform. During this time, the electron suffers from large accelerations to $\gamma > 300$ and decelerations to $\gamma \sim 100$ are seen for several times. Note that at this time, $t = 70.1$ fs, we see the intense radiation loss in Fig. 7(iii-d) around the position of the electron in Fig. 10. Therefore, the electron can be regarded as one of the sources of the intense radiation emission.

Third, in Fig. 11, trajectory of an electron from the first cluster is shown. In the case without radiation reaction, the electron escapes from the cluster to the $+y$ direction, turns to the $-y$ direction at position between the first and second clusters, and interacts with the laser field in the inter-cluster region just before the time $t = 70.1$ fs, which results in the quiver motion at around the front surface. The electron then begins to move ballistically toward the $+y$ direction. At $t = 70.1$ fs, we see a strong acceleration to $\gamma > 400$ at the position of initial surface of the first cluster. The similar acceleration to $\gamma > 400$ is seen also after the time at the second cluster position. These
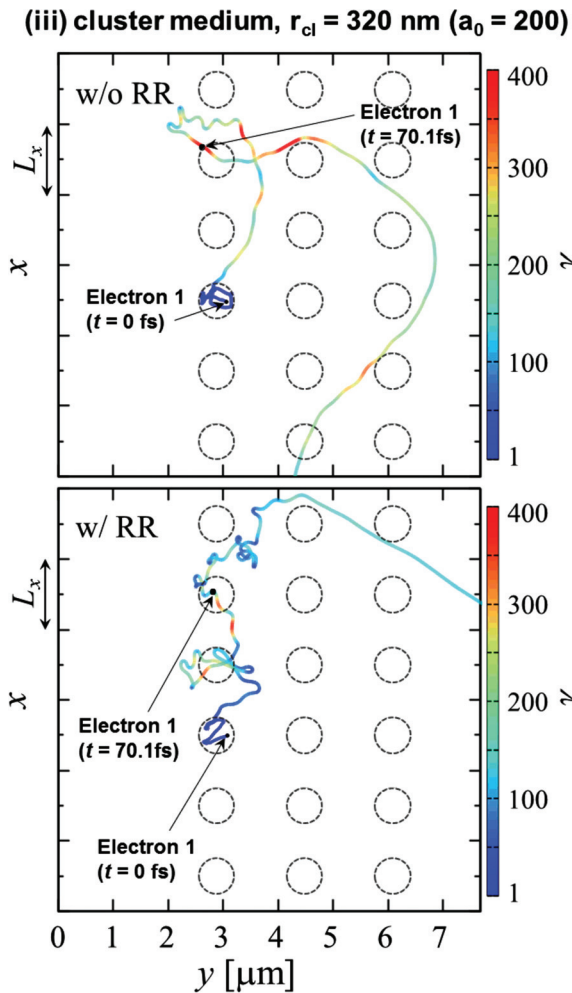
FIG. 11. Electron trajectory in cluster medium (iii) for $\hat{a}_0 = 200$ without (upper) and with (lower) radiation reaction. Circles with dashed line represent the initial position of clusters.

accelerations are attributed to the charge separation field created by the remaining ion cluster cores.

On the other hand, when the radiation reaction is taken into account, the trajectory becomes complex exhibiting non-ballistic trajectory that suffers strong accelerations and decelerations. This is considered to be due to the radiation reaction force which acts mainly to the $-\mathbf{v}$ direction as seen from the dominant third term in Eq. (7) and thus suppresses ballistic motions. We see that the electron is trapped by the neighboring cluster and suffers from accelerations for several times by the laser field and sheath field of the cluster. The electron then moves to the next cluster around the time $t = 70.1$ fs.

These accelerations and/or trappings by charge separation fields inside of cluster media is not seen for uniform media as case (i) where the sheath field is created only at the front and rear surfaces.

X. EFFECT OF RADIATION DAMPING IN ENERGY DISTRIBUTION

We further investigate the energy distributions for electrons and ions for the cases of uniform plasma (i) and cluster medium (iii) with $\hat{a}_0 = 200$.
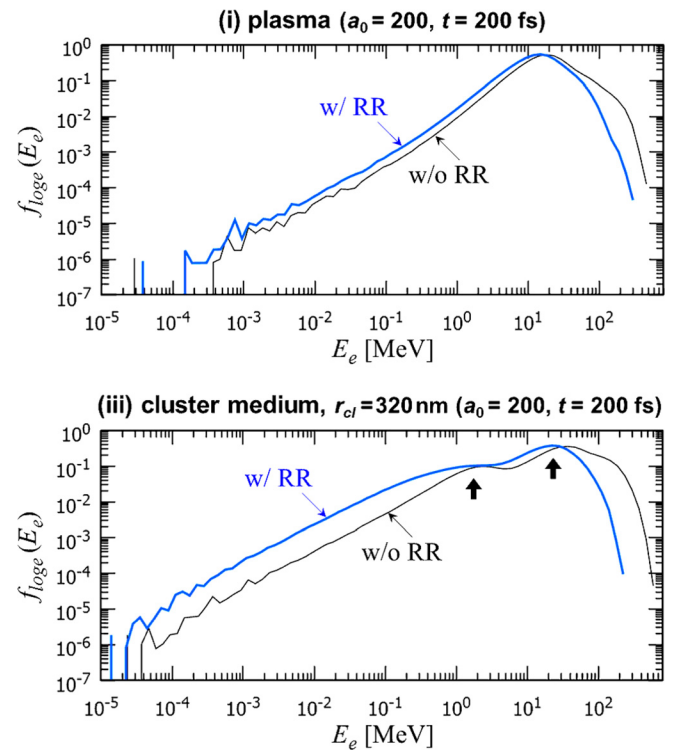

FIG. 12. Energy distributions of electrons for $\hat{a}_0 = 200$ without (black line) and with (bold blue line) radiation reaction. Upper and lower figures are for cases (i) and (iii), respectively.

First, in Fig. 12, we show the distributions of electron energy E_e at the time $t_{\mathrm{final}} = 200$ fs. The vertical axis is the normalized distribution function defined by $f_{\mathrm{loge}} = dN_e/d(\log E_e)/N_{\mathrm{etot}}$ where N_{etot} is the total number of electrons in the system so that $\int f_{\mathrm{loge}} d(\log E_e) = 1$. Upper and lower figures correspond to the cases of plasma (i) and cluster medium (iii), respectively. In each figure, results obtained from calculations without and with radiation reaction are shown by the black and bold blue lines, respectively. Note that the electron energy distribution for the cluster medium (iii) has two peaks indicated by bold arrows, one of which in the low energy regime denotes electrons that stay in clusters. Such a division of energy distribution is not seen in case (i), since whole electrons start to move being affected by the charge separation field in the continuous medium (i) as a return current.

For both cases (i) and (iii), the high energy component above $E_e = 100$ MeV is decreased largely due to the radiation damping by more than one order. The decelerated electrons distribute in the lower energy regime below 10 MeV where the distribution for the case with radiation damping shows higher value than that without radiation damping. These results denote that the radiation damping is effective especially for the high energy electrons with large relativistic factors, for which the dominant term of the radiation reaction force, i.e., the third term on the RHS on Eq. (7), becomes large.

In Fig. 13, we show ion energy distributions for cases (i) and (iii). Here, the vertical axis is the normalized distribution function defined by $f_i = F_i/\int F_i dE_i$ where $F_i = dN_i/dE_i/\sqrt{E_i}$ so that $\int f_i dE_i = 1$. We can also see the effect of radiation reaction on the high energy component in the ion energy
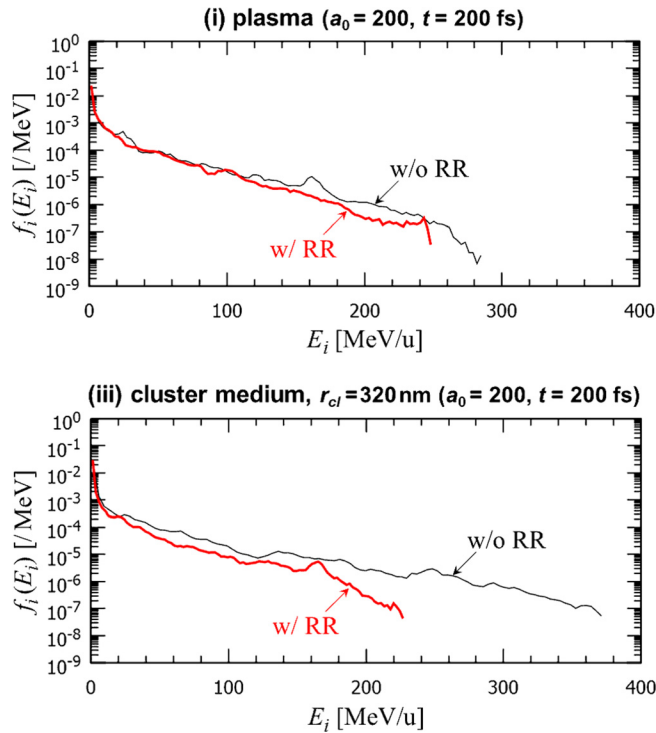
FIG. 13. Energy distributions of ions for $\hat{a}_0 = 200$ without (black line) and with (bold red line) radiation reaction. Upper and lower figures are for cases (i) and (iii), respectively.

distribution for both cases (i) and (iii). This is the indirect effect of the radiation reaction to ions, since the radiation reaction acts only on electrons and the ion acceleration takes place via electrons as we have seen in the energy evolution for electrons and ions in Fig. 6. Comparing Fig. 13 for (i) and (iii), we see that in the case without radiation reaction, the cluster medium (iii) generates more energetic ions whose maximum energy is larger by more than 80 MeV/u than that for plasma (i). However, the maximum ion energy in the cluster medium (iii) is decreased by the inclusion of radiation reaction to the same level of that in case (i), i.e., about 240 MeV/u. Therefore, it is found that the clustered structure enhances the ion acceleration when the radiation reaction is not taken into account; however, as the radiation reaction is included, the clustered structure enhances high energy radiation emission rather than the ion acceleration.

Note that for case $\hat{a}_0 = 100$, we confirmed that the relative difference of the maximum ion energy between cases without and with radiation reaction at $t = 200.1$ fs is less than 15%, and the maximum ion energy is still higher in the cluster medium (iii) than case (i) when the radiation reaction is taken into account.

XI. CONCLUSION

We studied the interaction between cluster media and high intensity laser fields in the radiation dominant regime assuming the laser peak amplitude of $\hat{a}_0 = 100$ and 200. Based on a theoretical estimation for the size of clusters that can interact with incident laser fields effectively while sustaining their property as the structured material, we introduced three kinds of targets with same total mass but have different

structures, i.e., uniform plasma and cluster media with two different cluster radii, in the two-dimensional PIC simulation. We investigated the effects of the internal structure of target materials on the interaction dynamics and radiation damping based on the PIC simulation that includes the radiation reaction to electrons in terms of the Landau–Lifshitz formula.

For both cases of $\hat{a}_0 = 100$ and 200, higher radiation energy loss rate, which corresponds to larger radiation emission, in the cluster media than that in the uniform plasma is found with enhancement of the incoherent component of the radiation friction. In the case of $\hat{a}_0 = 200$, the radiation rate is found to be 36% for the cluster medium assumed here, which is about three times higher than the radiation rate for the uniform plasma. The enhancement of radiation in the cluster media resulted from a wider spatial distribution of the radiation energy loss inside and front side area of the cluster media where electrons can interact directly with the intense laser field.

Electron trajectories in the cluster media are found to exhibit complex motions with less ballistic behaviors compared with the case of uniform plasma, due to accelerations and/or trappings by internal sheath fields created by clusters. Such an electron motion, which suffers from strong acceleration and then radiation friction for many times, results in the high radiation emission rate for the cluster media. The ion energy distribution is also found to be affected by the radiation reaction through the damping of the electron energy. As a result, the larger maximum ion energy achieved in the cluster medium is reduced by the inclusion of the radiation reaction to the same level with that in the uniform plasma. These results suggest that the clustered structure assumed here enhances the emission of high energy radiations rather than ion acceleration.

From the results obtained here, it is expected that the cluster media have a potential to create a high energy density state that is composed of relativistic electrons, intense laser field, and high energy radiations. The species of clusters (Z) will also be an important ingredient in determining the interaction such as cluster expansion and trapping of electrons to the cluster core, and even in considering the electron–positron pair production via the Bethe–Heitler and/or trident processes[40–42] using the created high energy density state. These issues will be studied in future work.

APPENDIX A: ENERGY CONSERVATION IN THE PIC SIMULATION INCLUDING THE RADIATION DAMPING

Here, we consider the energy conservation law in the simulation including the radiation damping.[33] We start from the energy density equation given by

$$\frac{\partial U_f}{\partial t} + \nabla \cdot \mathbf{S} = -\mathbf{E} \cdot \mathbf{J}, \tag{A1}$$

where $U_f = (E^2 + B^2)/8\pi$ is the field energy density, $\mathbf{S} = c\mathbf{E} \times \mathbf{B}/4\pi$ the Poynting vector, $\mathbf{E}$ the electric field, $\mathbf{B}$ the magnetic field, and $\mathbf{J}$ the current density. Here, since the laser field is excited by the external input of antenna current in our simulation, the current density $\mathbf{J}$ is composed of that of the antenna $\mathbf{J}_A$ and that generated by the plasma particles in the system $\mathbf{J}_p$, i.e., $\mathbf{J} = \mathbf{J}_A + \mathbf{J}_p$. The RHS of Eq. (A1) for the former component, i.e., $-\mathbf{E} \cdot \mathbf{J}_A$, represents the power input by the external antenna current. The latter component $\mathbf{J}_p$ can be determined by the energy equation for particle of species σ given by

$$\frac{d}{dt}\left(\gamma_\sigma m_\sigma c^2\right) = q_\sigma \mathbf{v}_\sigma \cdot \mathbf{E}(\mathbf{r}_\sigma) + \mathbf{v}_\sigma \cdot \mathbf{F}_{\text{rad}}(\mathbf{r}_\sigma), \tag{A2}$$

where q, γ, $\mathbf{r}$, and $\mathbf{v}$ are the charge, relativistic factor, position, and velocity of the particle, respectively. The first and second terms on the RHS of Eq. (A2) are originated from the Lorentz force and the radiation reaction force in the equation of motion Eq. (6), respectively. The plasma current density $\mathbf{J}_p$ is obtained as the sum of all the particles in the system as

$$\mathbf{J}_p(\mathbf{r}) = \sum_\sigma \sum_{i_\sigma=1}^{N_\sigma} q_{i_\sigma} \mathbf{v}_{i_\sigma} \delta(\mathbf{r} - \mathbf{r}_{i_\sigma}), \tag{A3}$$

where N_σ is the total number of particles of species σ.

We here consider averaging Eq. (A2) by the total volume V in order to obtain the energy conservation relation in the whole simulation system. For convenience, we introduce the notation $\langle A \rangle = \int_V A\, d\mathbf{r}/V$ and $\varepsilon_f = \langle U_f \rangle$. The averaged energy density equation is then expressed as

$$\frac{\partial \varepsilon_f}{\partial t} + \langle \nabla \cdot \mathbf{S} \rangle = -\langle \mathbf{E} \cdot \mathbf{J}_A \rangle - \langle \mathbf{E} \cdot \mathbf{J}_p \rangle. \tag{A4}$$

By using Eqs. (A2) and (A3), we calculate the second term on the RHS of Eq. (A4) as

$$-\langle \mathbf{E} \cdot \mathbf{J}_p \rangle = -\frac{1}{V} \int_V \sum_\sigma \sum_{i_\sigma=1}^{N_\sigma} q_{i_\sigma} \mathbf{v}_{i_\sigma} \delta(\mathbf{r} - \mathbf{r}_{i_\sigma}) \cdot \mathbf{E}(\mathbf{r}) dV$$
$$= -\frac{1}{V} \sum_\sigma \sum_{i_\sigma=1}^{N_\sigma} \left[\frac{d\left(\gamma_{i_\sigma} m_{i_\sigma} c^2\right)}{dt} - \mathbf{v}_{i_\sigma} \cdot \mathbf{F}_{\text{rad}}(\mathbf{r}_{i_\sigma}) \right]. \tag{A5}$$

Hereafter, we represent the averaged kinetic energy density as

$$\varepsilon_k = \frac{1}{V} \sum_\sigma \sum_{i_\sigma=1}^{N_\sigma} \gamma_{i_\sigma} m_{i_\sigma} c^2, \tag{A6}$$

and the averaged radiation power density as

$$w_{\text{rad}} = -\frac{1}{V} \sum_\sigma \sum_{i_\sigma=1}^{N_\sigma} \mathbf{v}_{i_\sigma} \cdot \mathbf{F}_{\text{rad}}(\mathbf{r}_{i_\sigma}). \tag{A7}$$

Then, the averaged energy density equation (A4) is rewritten as

$$\frac{\partial \varepsilon_f}{\partial t} + \frac{\partial \varepsilon_k}{\partial t} + \langle \nabla \cdot \mathbf{S} \rangle = -\langle \mathbf{E} \cdot \mathbf{J}_A \rangle - w_{\text{rad}}. \tag{A8}$$

This equation represents the energy conservation law for the simulation system that includes the laser field excitation by antenna and the radiation reaction force. The first and second terms on the LHS of Eq. (A8) are the time variation of field and kinetic energy densities in the system, respectively. The third term on the LHS corresponds to the Poynting power density flowing out of the system. On the RHS, note that $-\mathbf{E} \cdot \mathbf{J}_A > 0$ for antenna energy input and $w_{\text{rad}} > 0$ for damping of energy of the system by the radiation friction.

In obtaining the plots for time evolution of energy given in Figs. 4 and 6, we integrate Eq. (A8) in time and express the energy conservation relation at time t as

$$\varepsilon_f(t) + \varepsilon_e(t) + \varepsilon_i(t) + \int_0^t \langle \nabla \cdot \mathbf{S} \rangle dt + \frac{1}{2} \int_0^t \langle \mathbf{E} \cdot \mathbf{J}_A \rangle dt$$
$$- \varepsilon_{\text{in}}(t) + \varepsilon_{\text{rad}}(t) = \varepsilon_{\text{error}}(t). \tag{A9}$$

Here, ε_{rad} is the density of radiation energy loss defined by

$$\varepsilon_{\text{rad}} = \int_0^t w_{\text{rad}}\, dt. \tag{A10}$$

In Eq. (A9), we define the energy density of laser input as

$$\varepsilon_{\text{in}} = -\frac{1}{2} \int_0^t \langle \mathbf{E} \cdot \mathbf{J}_A \rangle dt. \tag{A11}$$

Here, we put $1/2$ on the RHS of Eq. (A11), taking into account that the half of the antenna current energy goes out immediately from the simulation system without any interaction for situations where the antenna is located near the boundary $y = 0$ with outgoing boundary condition as is assumed in this paper. Therefore, the half of the antenna current energy becomes the actual laser input energy to the system. Another half of the antenna current energy is then left as the fifth term on the LHS of Eq. (A9). On the RHS of Eq. (A9), we introduce the error of the energy conservation $\varepsilon_{\text{error}}$ which becomes zero in the ideal case without numerical errors. In Eq. (A9), the kinetic energy is divided into the electron and ion components as $\varepsilon_k = \varepsilon_e + \varepsilon_i$. Note here that, in the simulations presented in this paper, ε_{rad} includes only the radiation loss for electrons ($\sigma = e$) since we can neglect the radiation loss by ions as discussed in Sec. IV.

As an example, we plot each term of Eq. (A9) for the simulation of cluster medium (iii) with $\hat{a}_0 = 200$ in Fig. 14. Here, each value in Fig. 14 is normalized by the total antenna input energy up to the final time of simulation, $\varepsilon_{\text{in}}(t_{\text{final}})$, as same as in Fig. 6, e.g., $\tilde{\varepsilon}_f = \varepsilon_f/\varepsilon_{\text{in}}(t_{\text{final}})$. Note that Fig. 14 includes the actual Poynting energy density ε_{Poy}, i.e., the sum of the fourth and fifth terms on the LHS of Eq. (A9), and the error on the RHS of Eq. (A9), which are not shown in Fig. 6. Note also that, instead of the absorption energy $\tilde{\varepsilon}_{\text{abs}} = \tilde{\varepsilon}_e + \tilde{\varepsilon}_i$, we here plot $\tilde{\varepsilon}_{\text{tot}}$ that represents the sum of all terms except the sixth term ε_{in} on the LHS of Eq. (A9), i.e., $\tilde{\varepsilon}_{\text{tot}} = \tilde{\varepsilon}_f + \tilde{\varepsilon}_e + \tilde{\varepsilon}_i + \tilde{\varepsilon}_{\text{Poy}} + \tilde{\varepsilon}_{\text{rad}}$, for the purpose of confirming the balance relation with the antenna input energy.
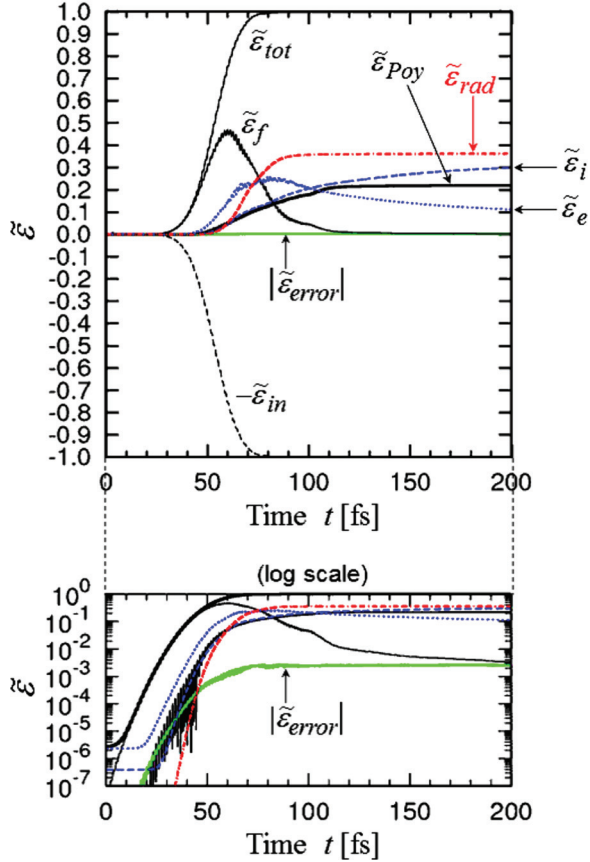
(iii) cluster medium, r_{cl} = 320 nm (a_0=200)

FIG. 14. Energy conservation relation among each term of Eq. (A9) normalized by the final value of the input energy density ε_{in} ($t = 200$ fs) for the case of cluster medium (iii) with $\hat{a}_0 = 200$. $\tilde{\varepsilon}_{Poy}$ denotes the sum of the fourth and fifth terms on the LHS of Eq. (A9). In the lower figure, region of positive $\tilde{\varepsilon}$ is shown in log scale.

It is seen in Fig. 14 that the minus value of the antenna energy $-\tilde{\varepsilon}_{in}$ is balanced with the sum of the other energies $\tilde{\varepsilon}_{tot}$. In the lower figure in the log scale, we see that the absolute value of the normalized error $|\tilde{\varepsilon}_{error}|$ shown by the green line is kept small in the order of $10^{-3} = 0.1\%$. Another simple example for the energy conservation assuming an underdense plasma is given in Ref. 33.

APPENDIX B: CALCULATION FOR RADIATION DENSITY DISTRIBUTION

In calculating the spatial distribution of radiation power density p_{rad} shown in Figs. 5 and 7, we first obtain the radiation energy loss during the simulation time step, i.e., $\Delta t = 0.0067$ fs, for each simulation cell as

$$\Delta\varepsilon_{rad}(t) = -\sum_{i=1}^{M_{sp}} \mathbf{v}_i(t) \cdot \mathbf{F}_{rad}(\mathbf{r}_i)\Delta t$$
$$= -\sum_{i=1}^{M_{sp}} \Delta\mathbf{r}_i \cdot \mathbf{F}_{rad}(\mathbf{r}_i), \quad (B1)$$

where M_{sp} is the number of super particle for electrons in the mesh, and $\mathbf{r}_i$ and $\mathbf{v}_i$ are the position and velocity of the i-th

super particle, respectively. We added the minus sign on the RHS so that $\Delta\varepsilon_{rad}$ becomes positive, taking into account that $\mathbf{F}_{rad}$ is considered to be a friction force, i.e., $\mathbf{v}_i \cdot \mathbf{F}_{rad} \leq 0$. The radiation power density p_{rad} in the unit of W/cm^3 can be obtained from $\Delta\varepsilon_{rad}$ as

$$p_{rad}(t) = \frac{n_{sav}V}{N_{sp}} \frac{\Delta\varepsilon_{rad}(t)}{V_{cell}\Delta t}. \quad (B2)$$

Here, V_{cell} is the volume of the cell, $n_{sav}V/N_{sp}$ corresponds to the number weight of the super particle where n_{sav} is the average density of electrons in the system, V the total volume of the system, and N_{sp} the total number of super particle for electrons.

[1]G. A. Mourou, T. Tajima, and S. V. Bulanov, Rev. Mod. Phys. **78**, 309 (2006).

[2]V. Yanovsky, V. Chvykov, G. Kalinchenko, P. Rousseau, T. Planchon, T. Matsuoka, A. Maksimchuk, J. Nees, G. Cheriaux, G. Mourou, and K. Krushelnick, Opt. Express **16**, 2109 (2008).

[3]T. Tajima and J. M. Dawson, Phys. Rev. Lett. **43**, 267 (1979).

[4]C. G. R. Geddes, Cs. Toth, J. van Tilborg, E. Esarey, C. B. Schroeder, D. Bruhwiler, C. Nieter, J. Cary, and W. P. Leemans, Nature **431**, 538 (2004).

[5]H. Hamster, A. Sullivan, S. Gordon, W. White, and R. W. Falcone, Phys. Rev. Lett. **71**, 2725 (1993).

[6]H. Hamster, A. Sullivan, S. Gordon, and R. W. Falcone, Phys. Rev. E **49**, 671 (1994).

[7]J. Galy, M. Maucec, D. J. Hamilton, R. Edwards, and J. Magill, New J. Phys. **9**, 23 (2007).

[8]K. W. D. Ledingham and W. Galster, New J. Phys. **12**, 045005 (2010).

[9]T. Nakamura, J. K. Koga, T. Zh. Esirkepov, M. Kando, G. Korn, and S. V. Bulanov, Phys. Rev. Lett. **108**, 195001 (2012).

[10]D. Stark, T. Toncian, and A. Arefiev, Phys. Rev. Lett. **116**, 185003 (2016).

[11]R. Kodama, P. A. Norreys, K. Mima, A. E. Dangor, R. G. Evans, H. Fujita, Y. Kitagawa, K. Krushelnick, T. Miyakoshi, N. Miyanaga, T. Norimatsu, S. J. Rose, T. Shozaki, K. Shigemori, A. Sunahara, M. Tampo, K. A. Tanaka, Y. Toyama, T. Yamanaka, and M. Zepf, Nature **412**, 798 (2001).

[12]T. Ditmire, J. Zweiback, V. P. Yanovsky, T. E. Cowan, G. Hays, and K. B. Wharton, Nature **398**, 489 (1999).

[13]T. Tajima, Scientific Advisory Committee: Report on the ELI Science (2009).

[14]D. Powell, Nature **500**, 264 (2013).

[15]S. V. Bulanov, T. Zh. Esirkepov, J. Koga, and T. Tajima, Plasma Phys. Rep. **30**, 196 (2004).

[16]J. Koga, T. Zh. Esirkepov, and S. V. Bulanov, Phys. Plasmas **12**, 093106 (2005).

[17]A. Zhidkov, J. Koga, A. Sasaki, and M. Uesaka, Phys. Rev. Lett. **88**, 185002 (2002).

[18]T. Ditmire, T. Donnelly, A. M. Rubenchik, R. W. Falcone, and M. D. Perry, Phys. Rev. A **53**, 3379 (1996).

[19]Th. Fennel, K.-H. Meiwes-Broer, J. Tiggesbäumker, P.-G. Reinhard, P. M. Dinh, and E. Suraud, Rev. Mod. Phys. **82**, 1793 (2010).

[20]M. V. Fomyts'kyi, B. N. Breizman, A. V. Arefiev, and C. Chiu, Phys. Plasmas **11**, 3349 (2004).

[21]S. V. Popruzhenko, M. Kundu, D. F. Zaretsky, and D. Bauer, Phys. Rev. A **77**, 063201 (2008).

[22]B. Shim, G. Hays, R. Zgadzaj, T. Ditmire, and M. C. Downer, Phys. Rev. Lett. **98**, 123902 (2007).

[23]T. D. Donnelly, T. Ditmire, K. Neuman, M. D. Perry, and R. W. Falcone, Phys. Rev. Lett. **76**, 2472 (1996).

[24]T. Tajima, Y. Kishimoto, and M. C. Downer, Phys. Plasmas **6**, 3759 (1999).

[25]S. V. Bulanov and V. S. Khoroshkov, Plasma Phys. Rep. **28**, 453 (2002).

[26]S. V. Bulanov, T. Zh. Esirkepov, V. S. Khoroshkov, A. V. Kuznetsov, and F. Pegorarod, Phys. Lett. A **299**, 240 (2002).

[27]Y. Fukuda, A. Ya. Faenov, M. Tampo, T. A. Pikuz, T. Nakamura, M. Kando, Y. Hayashi, A. Yogo, H. Sakaki, T. Kameshima, A. S. Pirozhkov, K. Ogura, M. Mori, T. Zh. Esirkepov, J. Koga, A. S. Boldarev, V. A. Gasilov, A. I.

Magunov, T. Yamauchi, R. Kodama, P. R. Bolton, Y. Kato, T. Tajima, H. Daido, and S. V. Bulanov, Phys. Rev. Lett. **103**, 165002 (2009).

[28]K. Nishihara, H. Amitani, M. Murakami, S. V. Bulanov, and T. Zh. Esirkepov, Nucl. Instrum. Methods Phys. Res., Sect. A **464**, 98 (2001).

[29]N. Iwata, Y. Kishimoto, R. Matsui, and Y. Fukuda, in Proceedings of IFSA, 2013.

[30]T. Esirkepov, M. Borghesi, S. V. Bulanov, G. Mourou, and T. Tajima, Phys. Rev. Lett. **92**, 175003 (2004).

[31]Y. Kishimoto, T. Masaki, and T. Tajima, Phys. Plasmas **9**, 589 (2002).

[32]L. D. Landau and E. M. Lifshitz, *The Classical Theory of Fields* (Pergamon, New York, 1994), Chap. 9.

[33]N. Iwata, Y. Kishimoto, Y. Fukuda, R. Matsui, H. Nagatomo, and H. Azechi, in Proceedings of the 14th Symposium on Advanced Photon Research, JAEA-Conf. 2015-001 (Japan Atomic Energy Agency, 2015), p. 76.

[34]B. N. Breizman, A. V. Arefiev, and M. V. Fomyts'kyi, Phys. Plasmas **12**, 056706 (2005).

[35]A. Arefiev, V. Khudik, A. P. L. Robinson, G. Shvets, L. Willingale, and M. Schollmeier, Phys. Plasmas **23**, 056704 (2016).

[36]J. D. Jackson, *Classical Electrodynamics*, 3rd ed. (John Wiley and Sons, New York, 1998), Chap. 14.

[37]J. Koga, Phys. Rev. E **70**, 046502 (2004).

[38]S. V. Bulanov, T. Zh. Esirkepov, M. Kando, J. K. Koga, and S. S. Bulanov, Phys. Rev. E **84**, 056605 (2011).

[39]T. Moritaka, L. Baiotti, A. Lin, L. Weiwu, Y. Sakawa, Y. Kuramitsu, T. Morita, and H. Takabe, J. Phys.: Conf. Ser. **454**, 012016 (2013).

[40]H. A. Bethe and W. Heitler, Proc. R. Soc. London, Ser. A **146**, 83 (1934).

[41]K. Nakashima and H. Takabe, Phys. Plasmas **9**, 1505 (2002).

[42]G. Sarri, K. Poder, J. M. Cole, W. Schumaker, A. Di Piazza, B. Reville, T. Dzelzainis, D. Doria, L. A. Gizzi, G. Grittani, S. Kar, C. H. Keitel, K. Krushelnick, S. Kuschel, S. P. D. Mangles, Z. Najmudin, N. Shukla, L. O. Silva, D. Symes, A. G. R. Thomas, M. Vargas, J. Vieira, and M. Zepf, Nat. Commun. **6**, 6747 (2015).